DISSERTATION

DEVELOPMENT OF ELECTROCHEMICAL IMAGING METHODS USING MICRO-ELECTRODE ARRAYS AND MICROFLUIDIC NETWORKS

Submitted by

John B. Wydallis

Department of Chemistry

In partial fulfillment of the requirements

For the Degree of Doctor of Philosophy

Colorado State University

Fort Collins, Colorado

Summer 2016

Doctoral Committee:

Advisor: Charles S. Henry

Alan Van Orden
B. George Barisas
Brian R. McNaughton
David S. Dandy

ABSTRACT

DEVELOPMENT OF ELECTROCHEMICAL IMAGING METHODS USING MICRO-ELECTRODE ARRAYS AND MICROFLUIDIC NETWORKS

Distribution of molecules over space and time drive a multitude of macroscopic and microscopic biological processes. There is a need to design novel imaging techniques that can map molecular distributions with spatiotemporal resolution. In this thesis, new electrochemical approaches to provide spatiotemporal imaging are presented. The bulk of this work utilizes high-density platinum micro-electrode arrays fabricated using complementary metal oxide semiconductor (CMOS) fabrication techniques as well as microfluidics and carbon-based electrodes fabricated using soft lithography fabrication techniques.

The systems described in this dissertation focus on quantification of biologically relevant neurotransmitters, mainly catecholamines and nitric oxide with concentration ranges from nM to mM. The pitch, or resolution between two “pixels” of electrochemical data, was 250 μm for microfluidic based sampling methods and 12.5 μm for the CMOS based sensors. Descriptions of fabrication methods for the carbon based electrodes and CMOS electrodes are described in this work. Finally, potential future directions of this technology is discussed in the final chapter.

ACKNOWLEDGEMENTS

First I would like to thank my advisor Dr. Chuck Henry for his mentorship and support throughout graduate school and the valuable opportunities he has provided me with. Next, I would like to thank Rachel Feeny for the enormous amount of research assistance and support she has provided during our time at Colorado State University together. I would also like to thank the many, professors, research scientists, post docs, graduate students and undergraduate students that have contributed to my research during graduate school, including Dr. Stuart Tobet, Dr. Tom Chen, Dr. David Dandy, Dr. Melissa Reynolds, Dr. Meghan Mensack, Dr. Jason Emory, Dr. Scott Noblitt, Dr. Murilo Santhiago, Dr. Thanakorn Pluangklang, Jaclyn Adkins, William Wilson, Tucker Kern, Yang Lang, Lei Wang, Valentina Pauna, Cody Eslinger, Chad Eitel, and Sean Morris. I would also like to thank my parents, sister, and Dr. Dwayne Hamar for their support during my entire education.

TABLE OF CONTENTS

CHAPTER 1. INTRODUCTION

Chemical gradients are important signaling phenomena in biology and give rise to a vast array of biological processes ranging from nerve signaling[1-3] to cell migration.[4-6] While optical imaging methods have been essential at elucidating these gradients, there are limitations to the molecules that can be seen. Additional imaging methods would improve our ability to image biologically-generated chemical gradients to further elucidate key biological functions of these gradients. This thesis investigates several electrochemical methods that allow quantitative spatiotemporal data to be obtained from dynamic chemical systems. First, carbon-based electrodes integrated into microfluidic devices are investigated as a means to generate, sample from, and quantify chemical gradients. Next, high-density microelectrode arrays are discussed as a platform for chemical gradient imaging. Integration of microfluidics with microelectrode arrays allows for precise fluid control and chemical gradient generation over the electrodes. Microfluidics have been used in previous work to both create and sample from chemical gradients.[7,8] Microelectrode arrays coupled with microfluidics have been reported previously,[9-11] but none have the number of electrodes and/or spatial resolution of the CMOS system described in Chapter Five. Also, on-chip potentiostats have only been utilized for a limited number of applications. Recently, an on-chip potentiostat was used for the detection of neurotransmitter release from chromaffin cells on a 10 × 10 electrode array.[9] Platinum ultramicroelectrode arrays of up to 36 electrodes in a 30 µm × 30 µm area have been used to make measurements across a single cell or cluster of cells.[10] The largest array reported here consists of 8,192 working electrodes in a 2 mm × 2 mm area and was designed to cover an area large enough to image a murine *ex vivo* tissue slice. Coupling our high-density electrode array with optical imaging methods has the potential to impact the understanding of how

molecular gradients drive biological phenomena such as chemotaxis, ovulation, neuronal growth, and cancer metastasis.

REFERENCES

1. K. Hong, M. Nishiyama, J. Henley, M. Tessier-Lavigne and M. Poo, *Nature*, 2000, **403**, 93-98.
2. H. Song, G. Ming and M. Poo, *Nature*, 1997, **388**, 275-279.
3. X. Cao and M. S. Shoichet, *Neuroscience*, 2001, **103**, 831-840.
4. S. Cheng, S. Heilman, M. Wasserman, S. Archer, M. L. Shuler and M. Wu, *Lab Chip*, 2007, **7**, 763-769.
5. Y. Luo and M. S. Shoichet, *Nat. Mater.*, 2004, **3**, 249-253.
6. S. H. Zigmond, *J. Cell. Biol.*, 1977, **75**, 606-616.
7. M. M. Mensack, J. B. Wydallis, N. S. Lynn, D. S. Dandy and C. S. Henry, *Lab Chip*, 2013, **13**, 208-211.
8. T. M. Keenan and A. Folch, *Lab Chip*, 2008, **8**, 34-57.
9. B. N. Kim, A. D. Herbst, S. J. Kim, B. A. Minch and M. Lindau, *Biosens. Bioelectron.*, 2013, **41**, 736-744.
10. J. Wang, R. Trouillon, Y. Lin, M. I. Svensson and A. G. Ewing, *Anal. Chem.*, 2013, **85**, 5600-5608.
11. I. A. Ges, R. L. Brindley, K. P. M. Currie and F. J. Baudenbacher, *Lab Chip*, 2013, **13**, 4663-4673.

CHAPTER 2. A SIMPLE MICROFLUIDIC ELECTROCHEMICAL HPLC DETECTOR FOR QUANTIFYING FENTON REACTIVITY FROM WELDING FUMES

Introduction

Development and characterization of a simple microfluidic electrochemical flow cell that can be coupled with HPLC to enable dual absorbance/electrochemical detection is described. Coupling absorbance and electrochemical detection increases the information that can be gathered from a single injection, but a second (typically expensive) detection system is required. Here, an inexpensive, customizable microfluidic electrochemical detector is coupled in series with a commercial HPLC-UV system. The microfluidic device is made from poly(dimethylsiloxane) and contains carbon paste electrodes. To demonstrate the utility of this dual detection system, the reaction products of the radical scavenging agent salicylic acid and hydroxyl radical generated by Fenton chemistry were analyzed. The dual-detection system was used to quantify 2,5-dihydroxybenzoic acid, 2,3-dihydroxybenzoic acid, and catechol produced by the addition of H_2O_2 to filter samples of welding fumes. Measurement recovery was high, with percent recoveries between 97–102%, 92–103%, and 95–103% for 2,5-dihydroxybenzoic acid, 2,3-dihydroxybenzoic acid, and catechol, respectively, for control samples. The methods described in this work are simple, reliable, and can inexpensively couple electrochemical detection to HPLC-UV systems. The development of the carbon paste electrodes in this work was used to make several electrochemical imaging devices described later in this thesis. The work described in this chapter was a collaborative effort by Thanakorn Pluangklang, who did the majority of the data collection, John Wydallis, who interfaced the device with the HPLC, and David Cate, who provided the welding fume samples. This work was published in *Analytical Methods*, Issue 20, in 2014.

Exposure to airborne environmental pollutants is a major worldwide health problem, listed as the 9th leading cause of morbidity and mortality in 2010 by the World Health Organization (WHO).[1] Common air pollutants include both molecular species and particulate matter (PM).

Reactive oxygen species (ROS) are present in and/or can be generated by aromatic compounds and transition metals found in particulate matter. ROS including H_2O_2, $^{\bullet}OH$, $RO_2^{\bullet}$, $O_2^{\bullet-}$, and NO are frequently monitored in air pollution due to their health effects.[2–8] Among the ROS, hydroxyl free radical ($^{\bullet}OH$, HFR) is particularly concerning because it reacts with DNA, membrane lipids, proteins, and carbohydrates and can lead to arthritis, cancer, cardiovascular disorders, stroke, and neurodegenerative diseases such as Alzheimer's and Parkinson's.[7–9] Measuring radical generation ability in PM is challenging because radicals are short lived and are often present in low abundance. One approach for measuring $^{\bullet}OH$ generation from PM is through radical trapping agents like salicylic acid. Salicylic acid reacts with $^{\bullet}OH$ to produce dihydroxybenzoic acid (DHBA) isomers that can be quantified using separation techniques such as high performance liquid chromatography (HPLC)[9–17] or capillary electrophoresis (CE) coupled with either UV or electrochemical detection (ECD).[18,19] Adding ECD to a HPLC-UV system results in a dual-detection system with more selectivity and specificity than either detection technique can provide alone.

HPLC is a common separation technique that has been used to analyze a wide range of organic and inorganic compounds. The most popular detectors used for HPLC separations are absorbance, fluorescence, refractive index, and conductivity detectors.[20] For electrochemically active compounds, ECD is useful because of its sensitivity and selectivity.[21,22] ECD can readily detect many molecular targets including phenols, aromatic amines,[21] glutathione,[22] reducing sugars,[23] antioxidants,[24,25] and thiols[26] by controlling electrode potential and/or electrode composition. Thus, electrochemistry has been widely demonstrated as a viable detection method for a variety of flow techniques including microfluidic applications. Microfluidic-ECDs have also been used in many applications ranging from microchip CE to microfluidic biosensors, covering a wide variety of clinical, pharmaceutical, immunosensor, biosensor, and measurement applications.[2,27–38] Microfluidic technology is amenable for shorter analysis times, lower reagent and sample consumption, higher portability, and lower material costs than other benchtop

methods. Generally, commercial electrochemical detectors provide wide linearity (3–4 orders of magnitude), low noise levels (nA–pA), high sensitivity (nM detection limits), and low response to flow, pressure, and temperature variations. However, commercial ECDs are usually expensive.[39] Therefore, it would be advantageous to fabricate inexpensive electrochemical flow cells whose geometry can be readily changed to reflect the specific application that can be directly coupled to HPLC instrumentation. Soft lithography coupled with inexpensive electrochemical detectors provides this opportunity.[2,26] These advantages spurred us to create a custom microfluidic-ECD that could be coupled directly to a commercial HPLC-UV system to demonstrate the utility of this analytical method.

This work presents a novel dual-detection HPLC-UV/ECD system built using a custom-made microfluidic ECD. This microfluidic system can be coupled to a commercially available HPLC system for determination of ˙OH generation from Fenton chemistry. Detection of Fenton reaction products using salicylic acid (SA) as the radical trapping agent was selected to demonstrate system applicability. The separation efficiency, sensitivity, and other analytical features of the custom ECD were studied as a function of the flow cell width and depth. Using the optimized system, ˙OH from PM samples was analyzed. Welding fume samples collected on filters were mixed with H_2O_2 and SA. The extraction parameters of the welding fume samples were optimized, and a recovery study of the welding fume samples was performed using the dual-detection system.

Experimental

Chemicals

All chemicals used in this study were analytical reagent grade and are given in the following list: salicylic acid (SA, Acros, USA), 2,3-dihydroxybenzoic acid (2,3-DHBA, Sigma-Aldrich, USA), 2,5-dihydroxy benzoic acid (2,5-DHBA, Sigma-Aldrich), acetic acid (Macron Chemicals, USA), sodium acetate (Sigma-Aldrich), citric acid (Fisher Scientific, USA), sodium

citrate (Fisher Scientific, USA), ferrous ammonium sulfate hexahydrate (Mallinckrodt, USA), 30% w/w hydrogen peroxide (H_2O_2, Fisher Scientific, USA), absolute ethanol (Sigma-Aldrich), pyro-catechol (Sigma-Aldrich), L-ascorbic acid (AA, Mallinckrodt), SU-8 negative photoresist (3050, 3025, and 2007) (Microchem, USA), 99% propylene glycol monomethyl ether acetate as developer agent (Sigma-Aldrich), Sylgard® 184 silicon elastomer base poly(dimethylsiloxane) monomer (PDMS, Dow Corning, USA), Sylgard® 184 elastomer curing agent (Dow Corning, USA), O122-1 heavy mineral oil (Fisher Scientific, USA), graphite powder, grade 38 (Fisher Scientific, USA), high-purity silver paint (SPI Suppliers, USA), tinned copper conductive wire (NTE Electronics, Inc., USA), and silicon wafers with 100-mm diameter and 500 ± 25 µm thickness (Silicon Inc., USA). All separations used HPLC grade solvents (EMD Chemicals Inc., Germany).

Microfluidic mold fabrication

Microfluidic chip fabrication was accomplished using standard soft lithography methods following established protocols.[2,26] Briefly, two molds were made on 100-mm diameter silicon wafers, one for the electrode channels (500-µm width, 50-µm depth, and 35-mm length) and one for the flow channel (250-µm width, 25-µm depth, and 35 mm length). The silicon wafer was cleaned with acetone, methanol, and water, dried with compressed air, and plasma cleaned (MSC plasma generator, USA) at 150 W at 0.8 torr for 5 min. Next the wafer was placed in a spin coater (WS-650MZ-23NPP/Lite, Laurell Technologies Corporation, USA) and 3–5 g of SU-8 (3050) was deposited on the wafer and spun at 3000 rpm for 30 s to achieve an SU-8 thickness of 50 mm. The wafer was then put on a hotplate to prebake at 95 ºC for 20 min. The desired mask pattern was placed over the photoresist on the wafer and exposed to UV light (OmniCure® Series 2000, Lumen Dynamics, Canada) at 50% intensity for 90 s. The post-exposure bake was performed at 95 ºC for 5 min. The development stage was completed by soaking the wafer in developer agent for 10 min followed by rinsing with acetone and drying with

compressed air. Finally, the wafer was baked at 195 ºC for 1 h. For the flow channel depth study, 25- and 12.5-µm channel depths used SU-8 3025 and SU-8 2007, respectively, instead of SU-8 3050, with 1000 rpm spin coating and 5 min pre-bake time following the same procedure as previously described.

Electrode platform construction and assembly of the coupled HPLC-UV/ECD system

The electrodes were made from a three-channel pattern with channel dimensions of 500-µm width, 50-µm depth, and 35-mm length that were subsequently filled with electrode material.[2,26] The channels were made by mixing PDMS at a ratio of 10 : 1 (w/w) of PDMS oligomer: cross linker followed by degassing with a vacuum pump (Vacuubrand, Germany) in a vacuum desiccator. The mixed PDMS was poured on the center of the mold surface slowly to prevent the addition of air bubbles and then baked at 80 ºC for 30 min. The electrode material was prepared as previously described by mixing PDMS and heavy mineral oil in a 1 : 1 ratio and then the binding material was mixed with graphite powder to get the final carbon paste electrode material. The electrode paste was spread into the PDMS channels and excess carbon paste removed using Scotch tape. The electrodes were baked at 65 ºC for 30 min. The electrode channels were refilled with carbon paste using the same procedure as stated above and then baked at 120 ºC for 1 h. Repeating this step improved electrode conductivity and thus the performance. The flow channels were fabricated using PDMS with the same procedure as described above. The flow channels had different dimensions of 12.5-, 25-, and 50-µm depths or 125-, 250-, 500- and 750-µm widths, and were all a length of 35-mm. The electrodes were exposed to air plasma at 150 W for 5 min. The flow channel and electrode layer were placed in 18-W plasma (PDC-32G Harrick, USA) for 20 s and then irreversibly sealed together by bringing the layers into conformal contact. Wires were connected to all electrodes using silver paint followed by covering the connections with epoxy to increase structural stability. A complete microfluidic electrode platform that can be coupled with the HPLC-UV system is shown in Figure

2.1. To make the connection between the HPLC UV detector and the ECD microchip, a 200-mm length of 0.0625 in PEEK tubing was inserted into a 1 mm hole made in the ECD *via* a tissue biopsy punch. Once the tubing was in place, the connection was reinforced by adding uncured PDMS to the opening. Once cured, this created an impermeable seal that prevented leakage around the tubing.

The HPLC (Thermo Scientific, Dionex Ultimate 3000 model and Chromeleon 7 software, USA) was coupled with a Poroshell 120 EC-C18 column, 2.1 × 150 mm, 2.7 µm (Agilent Technologies, USA), a binary gradient solvent system, and dual-detection setup. The detection setup consisted of a commercial multi-wavelength UV/Vis detector coupled in series with the microfluidic electrochemical detector (Figure 2.1). A portable potentiostat (EDAQ, EPU-352 model, IsoPod™ Biosensor with Pod-Vu software, Australia) was used for all electrochemical measurements. This detector was selected because of its low cost (<$800) and ease of connection to the HPLC control computer. All compounds were detected first by UV absorbance and then amperometry.

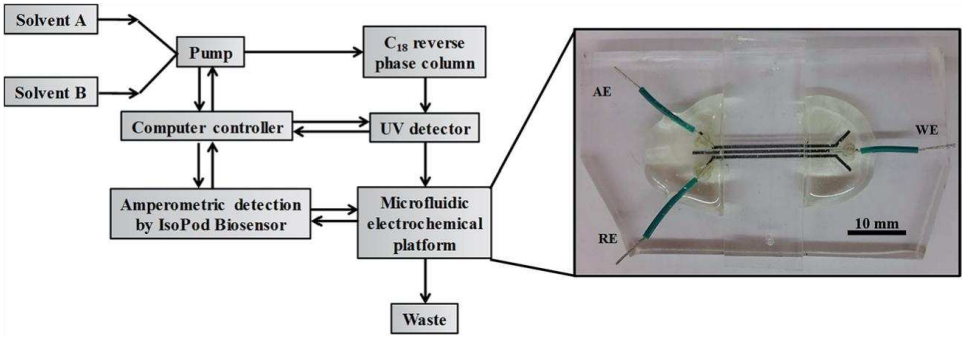

Figure 2.1: Scheme of the coupled microfluidic electrochemical detector with HPLC-UV, where AE = auxiliary electrode, WE = working electrode, and RE = reference electrode.

Application of the dual-detection system

In this work, Fenton chemistry was used to generate ˙OH followed by trapping it using salicylic acid.[9–18] In the first step in reaction (1), Fe(II) or a similar transition metal present in welding fume reacts with added H_2O_2.

$$Fe^{2+} + H_2O_2 \rightarrow Fe^{3+} + {}^{\cdot}OH + OH \quad (1)$$

The resulting ˙OH reacts with salicylic acid to produce three products,[9,16–18] shown schematically in reaction (2). In these experiments 42% catechol, 24.5% 2,5-DHBA, and 33.5% 2,3-DHBA was generated.

(2)

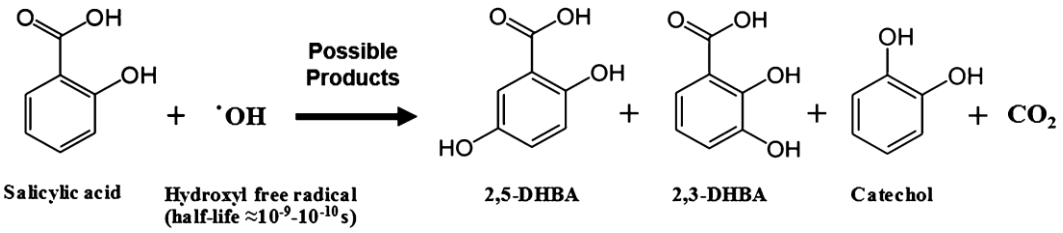

We elected to study this reaction because of our ongoing interest in measuring the oxidative load associated with aerosol exposure. The reaction is well suited for dual absorbance and electrochemical detection given the high oxidation potential of salicylic acid (>800 mV) *versus* that of the reaction products (300 mV). Combining both detection methods allows us to follow both product formation and reagent consumption simultaneously. Gradient elution was performed using a binary solvent system (modified from E. DiStefano *et al.*)[17] of 25 mM, pH 3.5 citrate buffer (solvent A) and acetonitrile (CH_3CN, ACN solvent B). For separation, a linear gradient from 5% (t = 0 min) to 50% (t = 5 min) ACN was used, followed by 50% ACN for 1 min. The column was re-equilibrated in 5% ACN for 10 min between each run. The optimal detection potential was determined using hydrodynamic voltammetry. When dual detectors were used, UV detection was performed at 280 nm and amperometric detection at +800 mV (*vs*. carbon paste pseudo-reference electrode). The elution time of each compound, the effect of applied potential on signal-to-noise ratio (S/N), linear range, and calibration curves for each of the Fenton reaction products were investigated using the dual-detection setup. The separation and detection of an additional reducing compound, ascorbic acid (AA), was also studied as it is commonly used with ˙OH generation studies.[17] The AA is used to reduce the Fe(III) to Fe(II). To demonstrate a field application, welding samples were collected on filters from laboratory

generated welding fumes and analyzed with the dual-detection system. Fumes were collected through mixed cellulose ester (MCE, Millipore, USA) membrane filters (0.8 µm pore size and 37 mm ø) at 4 L min^{-1} flow rate for 60 min. Samples no. 1–3 were collected through the MCE membrane with 4 L min^{-1} flow rate for 10 min while no. 4 was collected for 20 min. Then, a 5-mm diameter punch from each of the 4 samples was extracted by 500 µL DI water for 2 h.

For the recovery study, three experimental sets of 250 µL sample extract (set A), 250 µL sample extract with 25 µM Fe(II) (set B), and a standard 25 µM Fe(II) (set C) were separately prepared in 20 mM salicylic acid, 2 mM H_2O_2 in acetate buffer pH 5 for a total 1000 µL volume to perform the real Fenton reaction using 30 min reaction time. All solutions were injected into the HPLC for quantification. Fenton reaction product recovery was also investigated from the welding samples to support the validity of the proposed method.

Results and discussion

Optimization of separation and detection conditions

An optimal elution program was determined by injecting a mixture of ascorbic acid, 2,5-DHBA, 2,3-DHBA, catechol and salicylic acid (500 µM each). Isocratic elution was tested first using 5, 7.5, and 10% ACN, respectively. As expected, the elution time and resolution decreased with increasing ACN. Unfortunately, an optimized isocratic elution gave long separation times and significant peak tailing for salicylic acid (>20 min with 5% ACN isocratic elution). Therefore, a gradient elution was used for the separation. The optimal gradient started at 5% ACN and linearly increasing to 50% B within 5 min, held constant for 1 min before decreasing to 5% B in 1 min and held constant for 3 min using 10 min total running time. Using the optimized gradient elution, a baseline-resolved separation was possible in under 10 min. Figure 2.2 shows the elution order and dual-detection results obtained using the optimized gradient. The cause of the peak width increase for the ECD is unknown but is likely a combination of dead volume at the chip interface and differences in tubing diameters between

the UV and ECD detectors. In Figure 2.2, there is not a peak for salicylic acid in the ECD since salicylic acid is not detected at the potential used in these experiments. The differences in relative sensitivities between the two methods is also noteworthy and exhibits one of the advantages of the dual-detection approach.

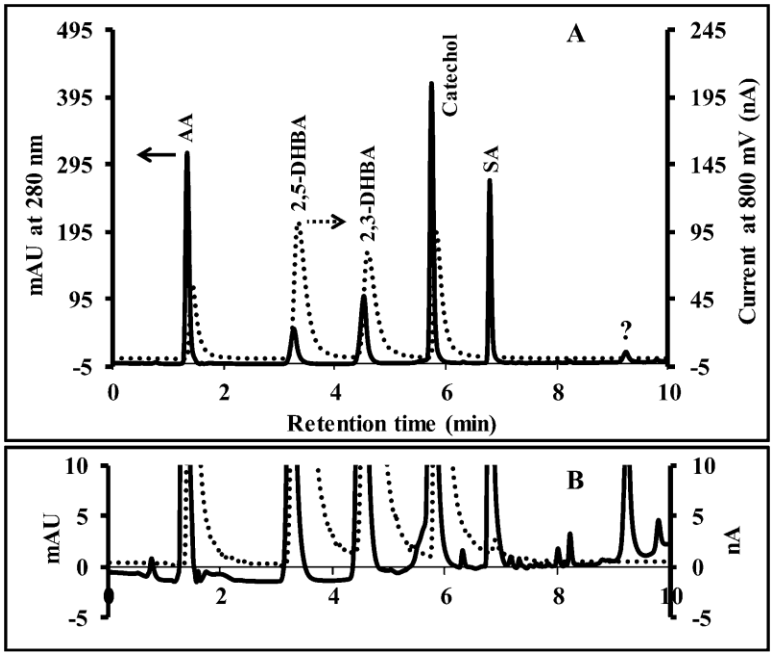

Figure 2.2: A) Chromatogram of Fenton reaction products using the dual-detection system. Dashed and solid lines represent amperometric detection and UV absorption signal, respectively. **B)** The differences in baseline between both detection methods. Separation conditions: column 2.7 µm Poroshell C_{18} (21 × 150 mm), injection volume of 10 µL, flow rate of 0.3 mL min^{-1}, mobile phase binary solvent system (A) 25 mM citrate buffer pH 3.5, and (B) CH_3CN, gradient elution starting at 5% B and linearly increasing to 50% B within 5 minutes, held constant for 1 min before decreasing to 5% B in 1 minute and held constant for 3 minutes (10 min run time).

Next, the S/N for electrochemical detection was investigated as a function of applied potential (Figure 2.3). From these results, the highest S/N ratio for all analytes except salicylic acid was in the range of 700–800 mV against a carbon paste pseudo-reference electrode. Higher applied potentials produced higher noise, thereby decreasing the S/N (Figure 2.3A). We selected 800 mV for amperometric detection to obtain the highest sensitivity for all of the analytes studied. Salicylic acid requires a

basic medium to be electrochemically active, and therefore is not detectable under our conditions.[40-42]

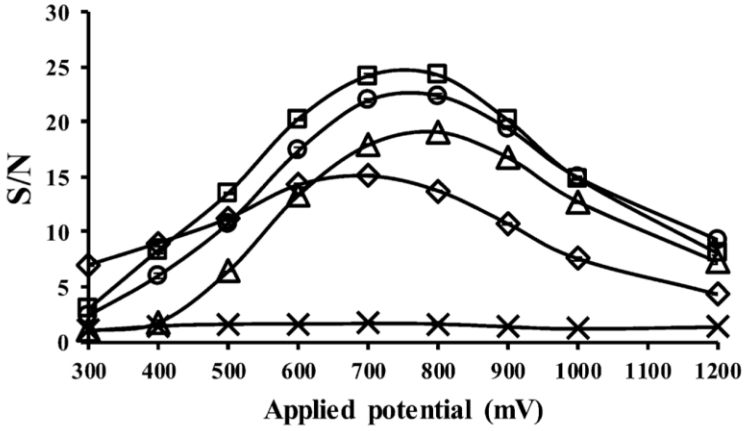

Figure 2.3: Voltage optimization study for all analytes, where (□) 2,5-DHBA, (O) catechol, (◊) ascorbic acid, (Δ) 2,3-DHBA, and (×) salicylic acid. Separation conditions were the same as stated in Figure 2.2.

Device optimization

The effect of channel width and depth was also investigated. The results are shown in Figures 2.4 and 2.5. In agreement with the Levich equation, better device sensitivity was obtained by increasing channel width or decreasing channel depth for all compounds, likely from an increase in the number of molecules in contact with the electrode surface.[43] Wider channels have a larger surface area for electrode contact and decrease the linear solution velocity (increasing residence time), and shallower channels decrease the average molecular diffusion distance to the electrode. The chromatographic separation efficiency, reported as plate number, N,[44] was calculated for catechol as a function of channel width and depth. The resolution between analyte pairs 2,5-DHBA/2,3-DHBA and 2,3-DHBA/catechol were in the range of 2.52–3.20 and 2.78–3.78, respectively. For future studies the channel design will be selected based on the relative importance of sensitivity and separation efficiency.

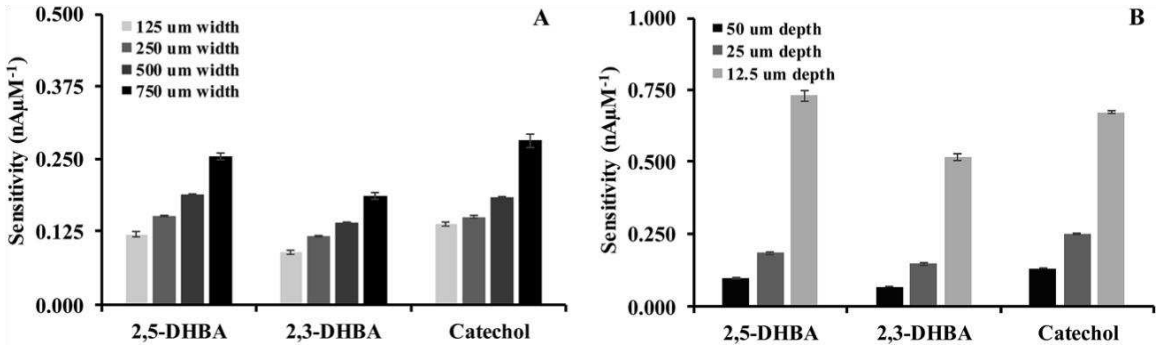

Figure 2.4: Effect of flow channel width and depth on the sensitivity of the analysis using **A)** constant 25-µm depth or **B)** constant 250-µm width. Separation conditions were the same as stated in Figure 2.2.

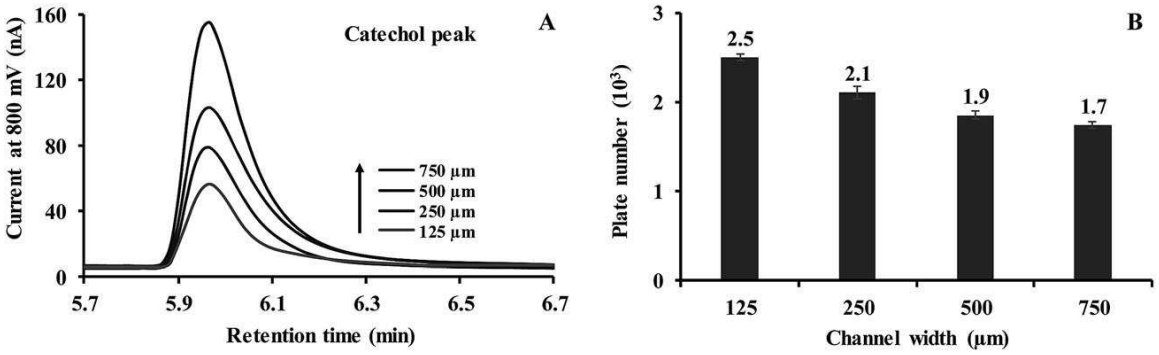

Figure 2.5: A) The observed peak shape for catechol as the ECD flow channel width is increased. Peak tailing is attributed to dead volume between the UV and ECD. **B)** The calculated plate number as the ECD flow channel width is increased. Separation conditions were the same as stated in Figure 2.2.

Analytical performance study

After determining the optimal conditions for the microfluidic electrochemical detector, we found that amperometric detection provided a slightly improved sensitivity relative to UV detection for the key components of the mixture. The results in Table 2.1 show the amperometric detector was able to measure the signal at the lowest concentration of 0.25 µM of catechol and both DHBA species, while UV absorbance was 0.50 µM. Conversely, UV detection gave a wider linear range for all compounds. We also investigated the theoretical detection limit[45] of all analytes by measuring the chromatogram peak height at a concentration of 0.50 µM

for all analytes using 10 replicates. The limit of detection (LOD) was calculated as three times the standard deviation divided by the calibration curve slope (3SD/slope), while 10SD/slope was used to calculate the limit of quantification (LOQ) from both UV absorption and amperometric signals (Table 2.1). For reproducibility, the relative standard deviation (% RSD) was calculated for 10 injections at 0.50 µM for all analytes. It was found that both reproducibility and detection limits of all compounds obtained from ECD were better than the UV detector. The improvements gained by the ECD can be attributed to the baseline drift of the UV signal caused by the gradient elution (see Figure 2.2B). The elution gradient did not cause a baseline drift in the electrochemical detector allowing it to achieve better performance metrics for this application. The S/N ratio for the ECD system increased as the exposed electrode area was increased as can be seen in Figure 2.4. The ECD could be used for >300 sample injections without cleaning before detrimental signal loss from electrode fouling was observed.

Table 2.1: The results of linearity, LOD, LOQ, reproducibility, and sensitivity studies using dual detectors.[a]

	Amperometric detection (peak current, nA)					UV absorption (peak height, mAU)				
Chemicals	Linear (µM)	LOD (µM)	LOQ (µM)	%RSD	Sensitivity (nA μM^{-1})	Linear (µM)	LOD (µM)	LOQ (µM)	%RSD	Sensitivity (mAU μM^{-1})
2,5-DHBA	0.25–125	0.11	0.37	0.77	0.4181	0.50–500	0.15	0.48	2.39	0.1068
2,3-DHBA	0.25–125	0.18	0.59	1.07	0.3506	0.50–500	0.19	0.63	3.67	0.2038
Catechol	0.25–125	0.23	0.77	1.43	0.3735	1.25–500	0.24	0.79	3.35	0.9296
SA	ND	ND	ND	ND	ND	0.50–500	0.05	0.17	0.86	0.6182

[a] ND = not detected.

Method application to Fenton reaction and welding fume sample analysis

Next, the dual-detection system was used to analyze the presence of ˙OH produced by Fenton chemistry. Various Fe(II) concentrations (0, 25, 50, 100 and 200 µM) were mixed with 20 mM salicylic acid and 2 mM H_2O_2 in acetate buffer (pH 5), and the resulting products were monitored after a 30 min reaction time. As expected, analyte generation and ascorbic acid consumption were dependent on the Fe(II) concentration. The H_2O_2 should not be retained by

the column and therefore it is likely the first small peak in the chromatogram. The peak current (pA) as a function of Fe(II) concentration (μM) showed a good linear relationship for 2,5-DHBA, 2,3-DHBA, and catechol giving a linear calibration of y = 3x + 3464 (r^2 = 0.9997), y = 6x + 3527 (r^2 = 0.9968) and y = 40x + 3088 (r^2 = 0.9998), respectively. These findings suggest that this technique can quantify ˙OH generated by Fenton chemistry.

For real sample analysis, laboratory generated welding fumes were generated using an electrode-arc generator. The welding sample extract without ascorbic acid did not generate peaks for catechol, 2,3-DHBA, or 2,5-DHBA. However, peaks did appear when 500 μM ascorbic acid was added to the reaction mixture, suggesting the metal content was already completely oxidized (predominately Fe(III)), and thus not reactive towards H_2O_2. The effect of extraction volume on extraction efficiency was also investigated (Table 2.2). The results showed that decreasing extraction volume increased current signal due to reduced dilution, while the signal of ascorbic acid also decreased simultaneously. The consumption of ascorbic acid had a linear relationship with the concentration of Fe(II). These results indicate that 500 μL DI water was optimal for sample extraction. Volumes of less than 500 μL were not tested because of the need to fully wet the filter membrane for extraction.

Table 2.2: Effect of extraction volume on extraction efficiency of welding filter sample.

	Current at 800 mV at various solvent volumes, mean ± SD ($n = 3$)			
Chemicals	1500 μL	1000 μL	750 μL	500 μL
Ascorbic acid	31.49 ± 1.26	19.62 ± 0.77	14.42 ± 0.31	8.96 ± 0.05
2,5-DHBA	4.35 ± 0.20	5.79 ± 0.16	7.55 ± 0.31	9.28 ± 0.04
2,3-DHBA	5.96 ± 0.15	8.05 ± 0.41	10.38 ± 0.27	12.23 ± 0.01
Catechol	7.46 ± 0.25	12.93 ± 0.79	16.06 ± 0.57	17.47 ± 0.66

The percent recovery of four welding fume samples was tested. The concentration of each analyte in the initial 500 μL extract was calculated to determine percent recovery, as

shown in Figure 2.6. Highly accurate results for all analytes were obtained from four different welding fume samples, confirming the reliability of the results obtained from the proposed microfluidic ECD system.

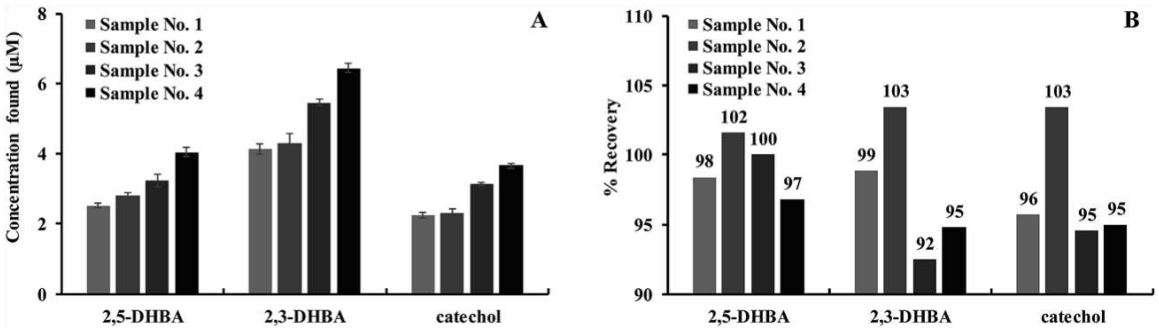

Figure 2.6: Welding fume **A)** sample analysis and **B)** percent recovery study (n = 3).

Conclusions

The custom-built ECD described here provides desirable characteristics including high sensitivity, high reproducibility, and ease of integration into commercial HPLC systems. The dimensions of the microfluidic channel over the electrodes can be quickly and inexpensively changed for different applications. For the analytes in this study it was seen that the custom microfluidic ECD was more sensitive and had higher reproducibility than the commercial UV detector on the HPLC system. Potential advantages of the dual-detection system include rapid peak identification, peak deconvolution, and rapid detector validation. In addition, further improvements in the detector design and electrode composition should make the ECD more sensitive than existing UV detectors for HPLC for a larger library of analytes. This proposed system can be applied for confirming the peak position in the same run between both detectors in case of complicated sample analysis. For some applications, we can use amperometry instead of UV absorption if an electrochemically inactive species is unable to completely separate from other electrochemically active compounds. Furthermore, multiple microfluidic

ECDs can be connected in series and different potentials can be applied to each set of electrodes for analyzing both oxidizable and reducible compounds in a single injection.

This work was supported by research grants to T. P. from the Royal Thai government Science and Technology Ministry Scholarship, National Science and Technology Development Agency (NSTDA) and the Center for Innovation in Chemistry: Postgraduate Education and Research Program in Chemistry (PERCH-CIC), Department of Chemistry, Faculty of Science, Mahidol University, Thailand. We also thank to the grant from National Institute of Environmental Health Sciences (NIH Grant ES019264).

REFERENCES

1. http://www.who.int/ceh/risks/cehair/en/.

2. Y. Sameenoi, K. Koehler, J. J. Shapiro, K. Boonsong, Y. Sun, J. J. Collett, J. Volckens and C. S. Henry, *J. Am. Chem. Soc*., 2012, **134**, 10562–10568.

3. M. Chevion, *Free Radical Biol. Med.,* 1988, **5**, 27–37.

4. M. Jiang, Q. Wei, N. Pabla, G. Dong, C. Y. Wang, T. Yang, S. B. Smith and Z. Dong, *Biochem. Pharmacol*., 2007, **73**, 1499–1510.

5. J. L. Zweier, S. S. Duke, P. Kuppusamy, J. T. Sylvester and E. W. Gabrielson, *FEBS Lett*., 1989, **252**(1, 2), 12–16.

6. H. Yamamoto, T. Watanabe, H. Mizuno, K. Endo, T. Hosokawa, A. Kazusaka, R. Gooneratne and S. Fujita, *Free Radical Biol. Med*., 2001, **30**(5), 547–554.

7. T. Obata, *Toxicol. Lett*., 2002, **132**, 83–93.

8. B. Ferger, P. Teismann, C. D. Earl, K. Kuschinsky and W. H. Lertel, *Pharmacol., Biochem. Behav*., 2000, **65**(3), 425– 431.

9. Application note “Measurement of The Hydroxyl Free Radical” ESA Analytical, Ltd., http://www.esainc.com/docs/ spool/701749P_Hydroxyl_Free_Radical.pdf, 1995.

10. D. R. McCabe, T. J. Maher and I. N. Acworth, *J. Chromatogr. B: Anal. Technol. Biomed. Life Sci*., 1997, **691**, 23–32.

11. W. N. Sloot and J. B. P. Gramsbergen, *J. Neurosci. Methods*, 1995, **60**, 141–149.

12. J. F. Jen, M. F. Leu and T. C. Yang, *J. Chromatogr. A*, 1998, **796**, 283–288.

13. A. J. Nappi and E. Vass, *Biochim. Biophys. Acta*, 1998, **1380**, 55–63.

14. A. J. Nappi and E. Vass, *Biochim. Biophys. Acta*, 1998, **1425**, 159–167.

15. D. Liu, J. Liu and J. Wen, *Free Radical Biol. Med.,* 1999, **27**, 478–482.

16. B. Liu and H. Wang, *J. Environ. Sci*., 2008, **20**, 28–32.

17. E. DiStefano, A. E. Fernandez, R. J. Delfino, C. Sioutas, J. R. Froines and A. K. Cho, *Inhalation Toxicol*., 2009, **21**(9), 731–738.

18. S. A. J. Coolen, F. A. Huf and J. C. Reijenga, *J. Chromatogr. B: Anal. Technol. Biomed. Life Sci.,* 1998, **717**, 119–124.

19. S. Ai, Q. Wang, H. Li and L. Jin, *J. Electroanal. Chem*., 2005, **578**, 223–229.

20. E. Kats, R. Eksteen, P. Schoenmakers and N. Miller, *Handbook of HPLC*, Marcel Dekker, Inc., New York, USA, 1998.

21. D. Parriott, *A Practical Guide to HPLC Detection*, Academic press Inc., California, USA, 1993.

22. I. Squellerio, D. Caruso, B. Porro, F. Veglia, E. Tremoli and V. Cavalca, *J. Pharm. Biomed. Anal.,* 2012, **71**, 111–118.

23. Y. G. Guan, P. Yu, S. J. Yu, X. B. Xu and X. L. Wu, *J. Dairy Sci*., 2012, **95**, 6379–6383.

24. M. Skrinjar, M. H. Kolar, N. Jelsek, A. R. Hras, M. Bezjak and Z. Knez, *J. Food Compos. Anal*., 2007, **20**, 539–545.

25. T. Vovk, M. Bogataj, R. Roskar, V. Kmetec and A. Mrhar, *Int. J. Pharm*., 2005, **291**, 161–169.

26. Y. Sameenoi, M. M. Mensack, K. Boonsong, R. Ewing, W. Dungchai, O. Chailapakul, D. M. Cropek and C. S. Henry, *Analyst*, 2011, **136**, 3177.

27. W. B. Zimmerman, *Chem. Eng. Sci*., 2011, **66**, 1412–1425.

28. J. R. Kraly, R. E. Holcomb, Q. Guan and C. S. Henry, *Anal. Chim. Acta*, 2009, **653**, 23–35.

29. C. D. Garcia and C. S. Henry, *Anal. Chim. Acta*, 2004, **508**, 1–9.

30. C. C. Hong, C. Y. Wang, K. T. Peng and I. M. Chu, *Biosens. Bioelectron*., 2011, **26**, 3620–3626.

31. F. Mostowfi, J. Czarnecki, J. Masliyah and S. Bhattacharjee, *J. Colloid Interface Sci*., 2008, **317**, 593–603.

32. C. H. Weng, W. M. Yeh, K. C. Ho and G. B. Lee, *Sens. Actuators, B*, 2007, **121**, 576–582.

33. W. Liang, Y. Li, B. Zhang, Z. Zhang, A. Chen, D. Qi, W. Yi and C. Hu, *Biosens. Bioelectron*., 2012, **31**, 480–485.

34. K. Islam, S. K. Jha, R. Chand, D. Han and Y. S. Kim, *Microelectron. Eng*., 2012, **97**, 391–395.

35. F. A. Bertolino, I. E. De Vito, G. A. Messina, H. Fernandez and J. Raba, *J. Electroanal. Chem*., 2011, **651**, 204–210.

36. J. Yang, J. H. Yu, J. R. Strickler, W. J. Chang and S. Gunasekaran, *Biosens. Bioelectron*., 2013, **47**, 530–538.

37. L. Y. Shiroma, M. Santhiago, A. L. Gobbi and L. T. Kubota, *Anal. Chim. Acta*, 2012, **725**, 44–50.

38. A. A. Dawoud, T. Kawaguchi, Y. Markushin, M. D. Porter and R. Jankowiak, *Sens. Actuators, B*, 2006, **120**, 42–50.

39. R. J. Flanagan, D. Perrett and R. Whelpton, *Electrochemical Detection in HPLC: Analysis of Drugs and Poisons*, The Royal Society of Chemistry, Cambridge, UK, 2005.

40. Z. Wang, F. Ai, Q. Xu, Q. Yang, J. H. Yu, W. H. Huang and Y. D. Zhao, *Colloids Surf., B*, 2010, **76**, 370–374.

41. W. D. Zhang, B. Xu, Y. X. Hong, Y. X. Yu, J. S. Ye and J. Q. Zhang, *J. Solid State Electrochem.*, 2010, **14**, 1713–1718.

42. I. Gualandi, E. Scavetta, S. Zappoli and D. Tonelli, *Biosens. Bioelectron*., 2011, **26**, 3200–3206.

43. R. G. Compton and P. R. Unwin, *J. Electroanal. Chem*., 1986, **206**, 57–67.

44. A. P. Sewell and B. Clarke, *Chromatographic Separation*, John Willey & Sons, London, UK, 1987.

45. D. C. Harris, *Quantitative Chemical Analysis*, W.H. Freeman and Company, New York, USA, 6th edn, 2003.

CHAPTER 3. SPATIALLY RESOLVED ELECTROCHEMICAL SENSING OF CHEMICAL GRADIENTS

Introduction

Chemical gradients drive a diverse set of biological processes ranging from nerve transduction to ovulation. At present, the most common method for quantifying chemical gradients is microscopy. Here, a new concept for probing spatial and temporal chemical gradients is reported that uses a multi-layer microfluidic device containing carbon electrodes to measure analyte concentration as a function of lateral position in a microfluidic channel in a format that is readily adaptable to multi-analyte sensing. The work described in this chapter was a collaborative effort by Meghan Mensack, who did a majority of the data analysis, John Wydallis, who constructed the devices and collected the data, and Scott Lynn, who designed the gradient generator and ran simulations. This work was published in *Lab on a Chip,* Issue 2, in 2013. The work described here is the initial project undertaken by the Henry lab for development of electrochemical imaging systems that have resolution over both space and time. The size of the electrodes used in this work is limited by the fabrication process and therefore the imaging system described in this chapter does not have as high resolution as the imaging systems described in Chapter Four and Chapter Five but the work in this chapter was an integral step in our lab's development of electrochemical imaging.

Measuring chemical gradients generated by biological systems is critical to understanding complex processes ranging from biological signaling to drug metabolism. Information on the release of biomarkers from living samples can (i) help elucidate the mechanisms of how different tissue/cell types interact with one another, (ii) demonstrate the effectiveness of pharmaceuticals on in vitro systems, and (iii) give rapid dose-response information when microfluidic chemical gradient generators are utilized.

Microscopy is the most common method for producing spatially and temporally resolved images of chemical gradients.[1-3] Unfortunately, microscopy is limited by the need to detect fluorescent or chemiluminescent molecules in biological systems. Other highly sensitive analytical techniques, including MALDI-MS, yield spatially resolved data of biomarkers at low concentrations on tissue and cell cultures;[4] however, the sample cannot survive the analysis process, making combined spatiotemporal analysis of living tissue difficult. A system that can spatially and temporally resolve the release of multiple non-fluorescent biomarkers from living tissue and cell cultures in near real-time would be desirable in the study of dose-response relationships, cellular communication mechanisms, and chronic toxicity studies.

In recent years, the use of microfluidic devices for the delivery of media to *in vitro* cell cultures has become a mainstay in cell biology, primarily due to the ability to provide precise control over both the composition of media as well as the dynamics of media delivery. Flow in microfluidic channels is generally confined to the laminar regime, where due to the small characteristic lengths and limited fluid velocities, Reynolds numbers are often well below one.[5] Laminar flow has been used to deliver concentration gradients of chemoattractants for chemotaxis studies of both mammalian and bacterial cells,[6-8] cytotoxic compounds for pharmacokinetic studies,[9] as well as small molecule gradients with subcellular gradient resolution.[10]

Electrochemical biosensors have many useful properties for measuring chemical gradients in cellular systems because they provide selectivity through either voltage control or surface modification and are capable of measuring low analyte concentrations. Furthermore, electrode arrays can be used to measure multiple analytes simultaneously. Carbon paste electrodes (CPEs) have been successfully applied in a broad range of biological applications because they resist biofouling and a have a large working potential range.[11,12]

This chapter describes the use of microfluidics to create and sample from a chemical gradient. Carbon paste electrodes similar to the electrodes described in Chapter Two were

utilized as the detection method for the dopamine gradients generated upstream of sampling ports aligned orthogonally to the gradient. This system has the potential to be used in the future to measure biomarker release from live cells or tissue slices with spatiotemporal resolution.

Results and Discussion

Here we have integrated CPEs into a multilayer microfluidic device to provide temporally and spatially resolved analysis of a single analyte as an initial step toward making measurements of biologically generated spatiotemporal chemical gradients from living tissue slices. The multilayer device (Figure 3.1) is capable of both generating and sampling chemical gradients. All three layers are fabricated from poly(dimethylsiloxane) (PDMS) using standard soft lithography processes.[13] Two syringe pumps are used to deliver liquid to a 2-channel input, 8-channel output gradient generator. The eight output channels of the gradient generator are introduced into a larger main chamber connected to the primary device outlet. A series of four vertical sample ports equally spaced in a line orthogonal to the fluid flow direction lead to four individual microchannels each oriented orthogonal to a 3-electrode CPE array. Electrodes were fabricated using graphite, carbon nanotubes, and a binding agent using previously published methods.[14]

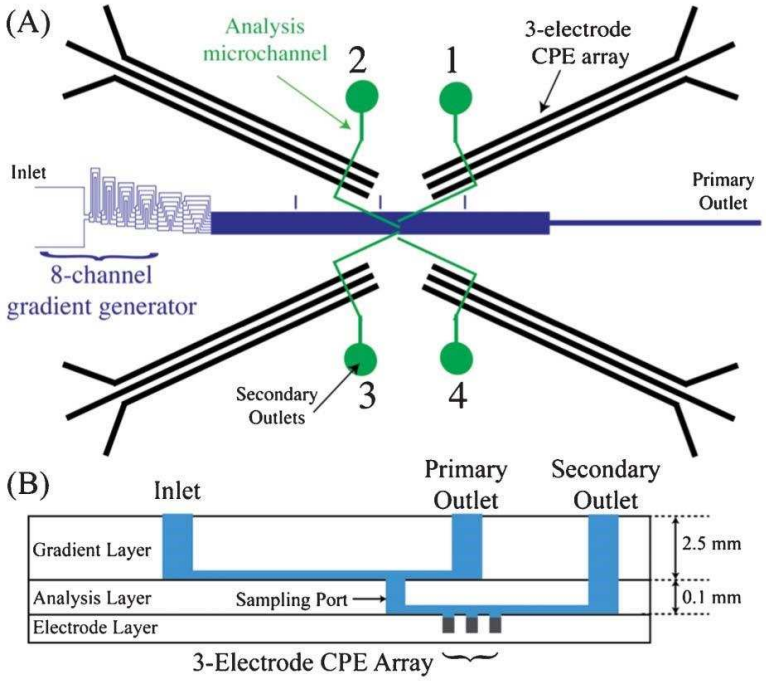

Figure 3.1: Diagram of the device used in this study. **A)** Top and **B)** side view of the three separate layers used within the device. All three layers are irreversibly bonded to one another. A 130-µm diameter punch is used to create the vertical sampling ports.

The viscous resistance of the system was designed such that, for pressure driven flow, 50% of the fluid will flow through the main chamber and exit through the primary outlet, and 12.5% of the fluid will flow through each analysis microchannel into a secondary outlet. With this design, the flow through the sample ports will have no effect on the shape of the upstream chemical gradient. The design of this system allows for continuous sampling from the 2-mm wide main chamber to monitor real-time changes in analyte concentrations from four distinct lateral locations. We have utilized the software package COMSOL to model the transport of both fluorescein and dopamine in this device, as shown in Figures 3.2 and 3.3.

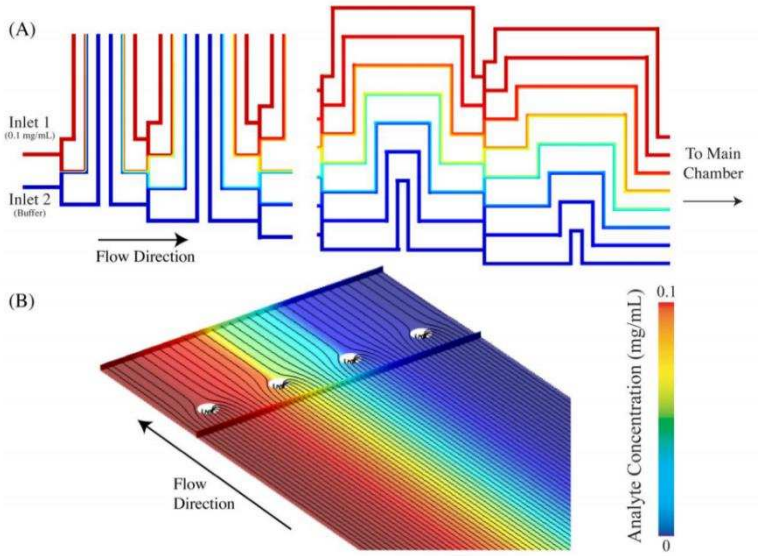

Figure 3.2: A) COMSOL simulation of the convection and diffusion of fluorescein within the gradient generator. The flow rates of each inlet stream are 10 µL min^{-1}, where one inlet has a concentration of 0.1 mg mL^{-1} of fluorescein. **B)** Contours of fluorescein and streamlines near the sample ports.

We have employed the use of the finite element package COMSOL to simulate transport of analyte through the topmost layer of the device. The flow rates through the microchannels are well within the Stokes regime, and the fluid is void of any turbulence. As a result, the convective and diffusive transport of analyte through the system can be modeled accurately *via* the solutions to both the Navier Stockes equations and the convection-diffusion equation. These simulations utilized a mesh with a characteristic size of 2.5 and 5 µm in the gradient generator and main chamber, which was predetermined such that the solution is independent of the mesh density. Typical 3D solutions consisted of over 300,000 hexahedral elements with 1.3 million degrees of freedom. The solution to the velocity, pressure, and concentration fields were obtained using the generalized minimal residual iterative solver, using a successive under-relaxation method for the pre- and post-smoother (with a PARDISO course solver). We employed a constant velocity condition on the two inlets, with the two inlets having an analyte concentration of 0 and 0.1 mg mL^{-1}, respectively. Because the simulation domain consisted only of the gradient layer, we employed a constant backpressure of p = 10 Pa on each analysis port

outlet (each outlet was extended 0.1 mm from the floor of the main chamber. This backpressure was chosen such that the volumetric flow rate exiting the primary outlet was 10 µL min^{-1}, with 2.5 µL min^{-1} flowing through each sample port. Solutions of this type were obtained for both fluorescein ($D = 5\times10^{-6}$ cm^2 s^{-1}) and dopamine ($D = 2.7\times10^{-6}$ cm^2 s^{-1}).

Figure 3.2A displays contours of analyte through the first and last sections of the gradient generator. As expected, the concentration of analyte decreases monotonically from top to bottom. The average fluorescein concentration in the eight outlet channels of the gradient generator (top to bottom) is 0.1, 0.096, 0.086, 0.068, 0.043, 0.020, 0.0057, and 0 mg mL^{-1}. Similarly, for dopamine these values are 0.26, 0.098, 0.09, 0.07, 0.041, 0.017, 0.003, and 0 mg mL^{-1}. The eight channels of the gradient generator enter the main flow chamber where diffusion orthogonal to the flow direction acts to smooth the chemical gradient before reaching the sample ports. Figure 3.2B displays the contours of analyte (fluorescein) along the floor of the microchannel in the region of the sample ports. Fluid streamlines (shown in black) are positioned 10 µm above the floor of the channel. It can be seen that the fluid near the channel floor will be drawn into a sample port situated directly downstream of the region in question. Therefore, the concentration in each analysis microchannel can be assumed to represent the concentration of analyte in the region just above each sample port.

From the results shown in Figure 3.2, we can calculate the average analyte concentration across the channel width situated 0.5 mm upstream of the sample ports. Figure 3.3 plots the average concentration of both fluorescein and dopamine across the channel width along with the average concentration of each analyte entering the four sample ports. These results parallel the experimental measurements for fluorescein (optical) and dopamine (electrochemical) seen in Figure 3.3. Because each sample port is collecting fluid within a radius larger than the characteristic size of each sample port, as seen in the fluid streamlines in Figure 3.2B, the average concentration in each port will be slightly higher than the concentration of analyte directly upstream of the center of each port. This effect can be resolved by decreasing

the flow rate through each analysis channel, accomplished by increasing the viscous resistance of the network of analysis microchannels (e.g. lengthening each channel).

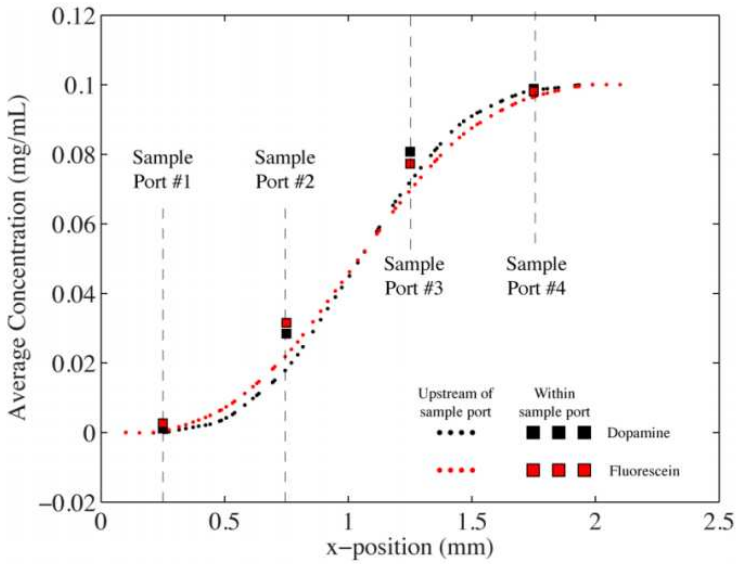

Figure 3.3: Average concentration of fluorescein and dopamine across the width of the main chamber (0.5 mm upstream of the sample ports). This data was taken from the results shown in Figure 3.2. The average concentration of both analytes entering each sample port is also shown.

The multilayer approach taken in this study is preferred over placing electrodes directly into the main chamber because it isolates the bulk of each electrode from the chamber and allows for multiple analytes to be quantified from the same spot using expandable electrode arrays.

We utilized time-dependent injections of dopamine to test the ability of the underlying CPE arrays to provide temporal and spatial characterization of chemical gradients present in the main chamber. Two syringe pumps were used to pump phosphate buffered saline (PBS, 1X) solution in equal proportions into each inlet (10 µL min^{-1} per pump). A two-way, six-port valve with a 10 µL injection loop was then used to introduce dopamine solutions of varying concentrations into one side of the gradient generator. The gradient generator has been designed such that upon injection dopamine will be transported through each microchannel (in each successive branch of channels) at similar rates. Therefore, the concentrations of dopamine

passing over each sample port will be proportional to one another, and furthermore, that proportionality will not be a function of time.

After injection, dopamine was detected amperometrically on each CPE electrode array *via* the oxidation of dopamine to dopamine-*o*-quinone (0.6 V applied potential *vs*. carbon paste pseudo reference electrode), resulting in a time-series current recording for each sample port. The peak current for all sampling ports with respect to the amperometric detection of decreasing concentrations of dopamine in 1X PBS is shown in Figure 3.4. As expected, the peak current decreases with decreasing dopamine concentration. Furthermore, the peak current also decreases with decreasing sample port number, where the proportionality of the responses across all sample ports is not a function of injection concentration. Plots of time-series injections for the five different concentrations seen in Figure 3.4 can be found in Figure 3.5. The inset in Figure 3.4 displays the time-series response to all four CPE arrays for a dopamine injection of 250 µM. The overall length from the injector to the sample ports is approximately 125 mm (compared to only 7.3 mm from each sample port to CPE array), and it may be assumed that the axial dispersion seen in the inset of Figure 3.4 is primarily a result of the longer channels upstream of the ports.[15] Therefore, we can infer a relationship between the peak current on each electrode and the concentration of dopamine passing over each sample port.

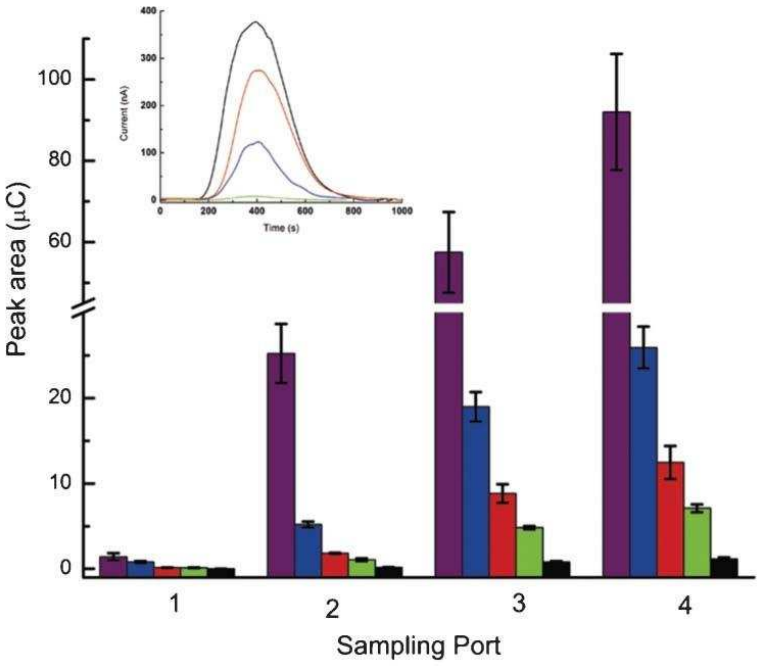

Figure 3.4: Peak area *vs.* sampling port for dopamine concentrations (10 μL injections) of 1 mM (purple), 250 μM (blue), 100 μM (red), 50 μM (green), and 10 μM (black). The error bars represent the standard deviation of three separate injections at each concentration. Inset: Current *vs.* time for a single 250 μM injection of dopamine for all four sample ports.

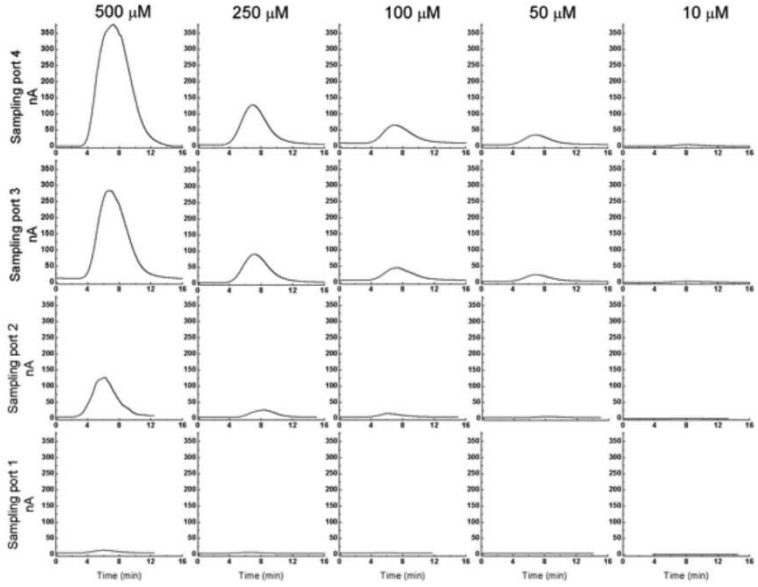

Figure 3.5: Signal vs. time for the spatial and temporal electrochemical detection of dopamine.

Figures 3.4 and 3.5 demonstrate the ability of this device to sample a chemical gradient in four separate locations. Unfortunately, due to the effects of diffusion, the shape of the dopamine gradient near the sampling ports cannot be predicted analytically. To determine the overall shape of a chemical gradient created in this device, fluorescein was added to one of the inputs (0.1 mg mL^{-1}) and the system analyzed using fluorescent microscopy. Because fluorescein ($5 \times 10^{-6}\,cm^2\,s^{-1}$) and dopamine ($2.7 \times 10^{-6}\,cm^2\,s^{-1}$) have similar diffusivities, the experimental shape of the fluorescein gradient will be similar to a dopamine gradient tested under the same conditions (buffer composition, flow rate). This similarity has been confirmed with COMSOL, where the concentration profile across the width of the channel is detailed in Figures 3.2 and 3.3. Figure 3.6A displays a fluorescent image of a steady-state fluorescein gradient in the vicinity of the four sample ports, and it can be seen that the fluorescein concentration decreases monotonically across the width of the channel. These data agree well with the COMSOL predictions, both for the fluorescein and dopamine results.

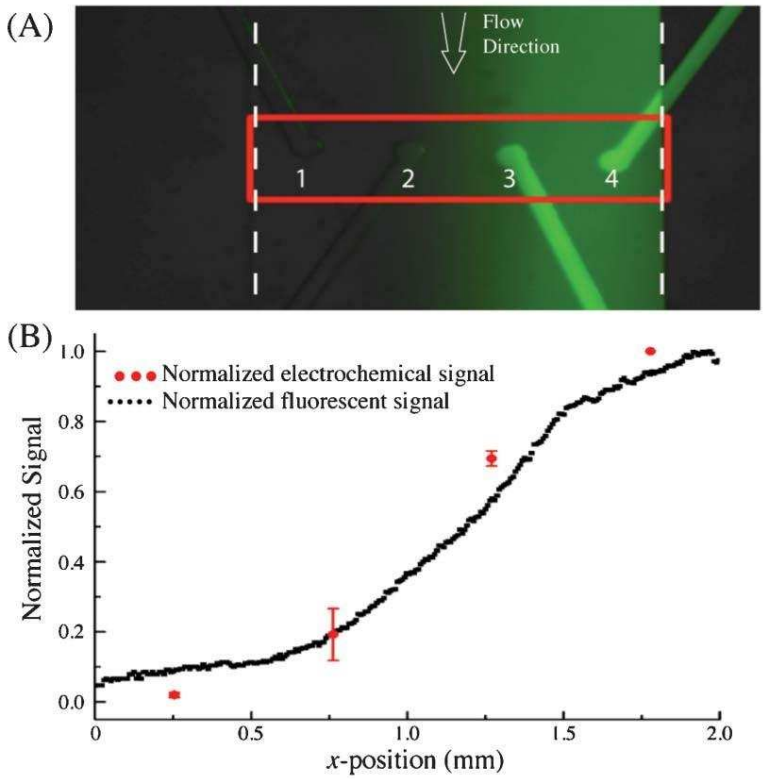

Figure 3.6: A) Fluorescent micrograph of gradient at sampling ports (2.3 cm from gradient network outlet). Dashed white lines indicate fluidic channel walls. Red box indicates the location of the four 130 µm diameter vertical sampling ports. Numbered from left to right, ports 1–4 are at 0.25, 0.76, 1.27, and 1.78 mm from the left channel wall, respectively. **B)** Comparison of the normalized fluorescent intensity *vs*. x-position taken from image in A (black points) to the normalized signal obtained from the detection of dopamine by the CPE array (red points).

To allow for direct comparison with the fluorescent line scan data, the signal at each set of electrodes was normalized to the signal at port 4, which was the highest magnitude for each of the five concentrations. The four port values for each concentration were then averaged and reported here as the mean ± SD. Likewise, the fluorescent data was normalized to the maximum intensity across the channel and plotted as a function of x-position (distance across the main chamber). As seen in Figure 3.6B, there is good agreement between the fluorescent line scan and the amperometry data collected from the device. It should be noted that the amperometric data represents replicate injections at five different concentrations of dopamine.

The slight deviations between the fluorescent and amperometric data shown in Figure 3.6B can perhaps be attributed to the 1.96 difference in diffusivity between fluorescein and

dopamine. The lower diffusivity of dopamine results in less band broadening of the overall gradient (across the width of the channel), resulting in lower and higher concentrations at the left and right side of the channel, respectively, when compared to a fluorescein gradient.

The dopamine detection limit in this system was determined by injecting homogeneous concentrations of dopamine through both of the gradient introduction ports. The chemical gradient in the main flow channel is eliminated and a uniform concentration of dopamine at each sampling port is established. Using this method, the lowest detectable dopamine concentration (S/N = 3) was found to be 250 nM. This detection limit is high relative to other hybrid microfluidic electrochemical systems due to several factors.[14] First, the laminar flow through the gradient generator will contribute to a measurable level of axial dispersion. Second, the electrode channels were not completely filled with carbon paste, resulting in the potential for analyte flow over the broader electrode and increased baseline noise. In the future, this limitation will be addressed *via* improved fabrication methods. By doing this, we anticipate being able to achieve detection limits closer to that seen previously (<10 nM) with similar CPEs.[16] Regardless of the current detection limits, spatiotemporal gradients in dopamine were measured effectively and these provide a solid foundation for future measurements of biologically generated gradients.

Conclusions

The microfluidic carbon-microelectrode system described here demonstrates the ability of this sampling method to measure the spatial and temporal distribution of both fluorescent and electrochemically active molecules within a fluidic gradient system. While only four sampling ports were used in this proof of concept device, the position of each sampling port can be accurately modified to sample liquid from specific regions of interest. We are presently incorporating cell cultures into this system and using a gradient to deliver compounds with known biological activity to monitor changes in extracellular metabolites. This new system will help quantify dose-response relationships between drugs and tissue/cell cultures more rapidly

than traditional microplate methods. Furthermore, it will allow us to gain insight into the intricate biological signaling mechanisms involved in cellular response to external chemical stimuli and allow us to spatially resolve small molecule release and movement during tissue development. It should also be noted that due to the design of the underlying microfluidic layer, this type of device could be used with most detection methods using a planar design, including optical, mechanical, or other electrochemical methods.

Preliminary Tissue Results

To test imaging with spatiotemporal resolution from a live tissue slice, a simplified microfluidic device with only two sampling ports and two electrode arrays was constructed as seen in Figure 3.7. Murine ovarian slices (250 µm thickness) were sectioned from a live ovary by the Tobet lab, mounted on a 10-mm diameter nylon mesh disc, and placed over the two sampling ports on the microfluidic device. The baseline amperometric signal was collected, and then the ovary slice was stimulated to release catecholamines by introducing a 55 mM KCl solution to the top of the ovary slice. The released catecholamines were detected by the downstream electrodes after a period of approximately 23 minutes Figure 3.8.

A) B)

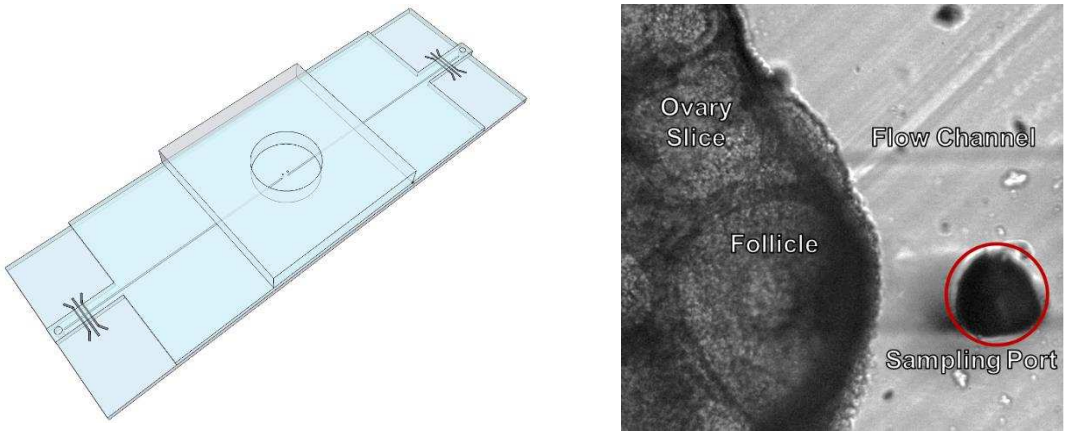

Figure 3.7: A) Schematic of the tissue sampling microfluidic device designed to fit on a standard 25 mm × 75 mm glass microscope slide. The two small 100-µm diameter sampling ports can be seen in the center of the device. The well surrounding the ports was 10 mm in diameter and was designed to hold the nylon disc that had the tissue mounted on it. The two discrete electrode arrays can be seen on either side of the device. **B)** A microscopy image of the ovary slice mounted above the sampling ports. The 100-µm diameter sampling port and sampling channel can be seen on the right side of the image.

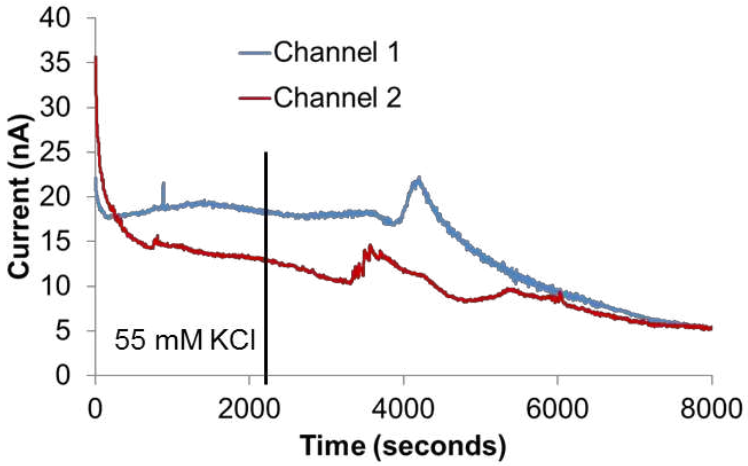

Figure 3.8: Amperometry data showing the stimulated catecholamine release from a murine ovary slice. At 2100 seconds a 55 mM solution of KCl was added to the top of the ovary slice to stimulate catecholamine release. The addition of KCl is indicated by the vertical black line. The blue and red traces represent the amperometry data collected from the right and left sampling ports respectively. Signal increase can be seen starting at 3500 seconds indicating the detection of catecholamine oxidation.

This preliminary data of the detection of catecholamine release from a live tissue slice suggests that tissue slices can be kept viable within a microfluidic sampling device, the microfluidic ports can give the data both spatial and temporal resolution, and the carbon-based electrodes are a suitable detection method for the measurement of catecholamines.

REFERENCES

1. D. A. Williams, K. E. Fogarty, R. Y. Tsien and F. S. Fay, *Nature*, 1985, **318**, 558-561.

2. J. Q. Zheng, M. Felder, J. A. Connor and M. Poo, *Nature*, 1994, **368**, 140-144.

3. B. G. Chung, L. A. Flanagan, S. W. Rhee, P. H. Schwartz, A. P. Lee, E. S. Monuki and N. L. Jeon, *Lab Chip*, 2005, **5**, 401-406.

4. R. L. Caldwell and R. M. Caprioli, *Mol. Cell. Proteomics*, 2005, **4**, 394–401.

5. J. Pihl, M. Karlsson and D. T. Chiu, *Drug Discovery Today*, 2005, **10**, 1377–1383.

6. H. Mao, P. S. Cremer and M. D. Manson, *Proc. Natl. Acad. Sci. U. S. A*., 2003, **100**, 5449–5454.

7. N. Li Jeon, H. Baskaran, S. K. W. Dertinger, G. M. Whitesides, L. Van De Water and M. Toner, *Nat. Biotechnol*., 2002, **20**, 826–830.

8. I. Barkefors, S. B. Le Jan, L. Jakobsson, E. Hejll, G. Carlson, H. Johansson, J. Jarvius, J. W. Park, N. Li Jeon and J. Kreuger, *J. Biol. Chem*., 2008, **283**, 13905–13912.

9. J. Pihl, J. Sinclair, E. Sahlin, M. Karlsson, F. Petterson, J. Olofsson and O. Orwar, *Anal. Chem*., 2005, **77**, 3897–3903.

10. S. Takayama, E. Ostuni, P. LeDuc, K. Naruse, D. E. Ingber and G. M. Whitesides, *Nature*, 2001, **411**, 1016–1016.

11. A. Morrin, A. J. Killard and M. R. Smyth, *Anal. Lett*., 2003, **36**, 2021–2039.

12. M. Pumera, A. Merkoci and S. Alegret, *Electrophoresis*, 2007, **28**, 1274–1280.

13. Y. Xia and G. M. Whitesides, *Angew. Chem., Int. Ed*., 1998, **37**, 550–575.

14. J. J. P. Mark, R. Scholz and F.-M. Matysik, *J. Chromatogr., A*, 2012, **1267**, 45–64.

15. G. Taylor, *Proc. R. Soc. London, Ser. A*, 1953, **219**, 186–203.

16. Y. Sameenoi, M. M. Mensack, K. Boonsong, R. Ewing, W. Dungchai, O. Chailapakul, D. M. Cropek and C. S. Henry, *Analyst*, 2011, **136**, 3177–3184.

CHAPTER 4. ANALYSIS OF NITRIC OXIDE FROM CHEMICAL DONORS USING CMOS PLATINUM MICROELECTRODES

Introduction

Electrochemical detection of NO generated from chemical donors is reported. Because NO is an important biological messenger, many donor sources and detection methods have been developed. Few reports have characterized NO donors using electrochemistry despite electrochemical techniques being sensitive and selective. Here, a CMOS platinum microelectrode array is interfaced with a microfluidic device for the electrochemical analysis of NO from (*Z*)-1-[*N*-(2-aminoethyl)-*N*-(2-ammonioethyl)amino]diazen-1-ium-1,2-diolate (DETA/NO). The donor parent amine fouls the electrode, resulting in substantial signal loss, but an electrochemical cleaning method was developed that substantially reduces fouling and allows detection of NO between 90 nM and 1 µM. The knowledge gained from this work helped us to understand how to interface microfluidics with CMOS microelectrode arrays for biomarker detection. This work was published in *Electroanalysis*, Issue 5, in 2015. This work was a collaborative effort between Rachel Feeny, who did the majority of the data collection and analysis, and John Wydallis, who designed and built the microfluidics.

Nitric oxide (NO) has a significant impact in biological systems through its role in cellular signaling by promoting vasodilation,[1] wound healing,[2, 3] and angiogenesis.[4, 5] Additionally, NO is involved in neurotransmission[6] and has antibacterial properties.[7] Of particular interest is the role of NO in directing cell migration,[8, 9] proliferation, survival, and differentiation.[10]. Simultaneously monitoring NO release from tissue while observing the cells could help in the understanding of how NO drives cellular processes. NO detection can be challenging, however, due to its short aqueous lifetime.[1, 6] Samples for laboratory studies are typically generated by bubbling NO gas through water to make a saturated solution, reducing nitrate or nitrite in solution to form NO, or by using a NO-releasing compound.[11] NO-releasing compounds can provide long-term,

constant NO release, allowing samples to be easily prepared and generate steady state NO concentrations. Many NO donors have been synthesized, and decompose through various mechanisms to generate NO. S-nitrosothiols can decompose through a variety of mechanisms, including catalysis by Cu^{+}, light, and pH, and NONOates (1-substituted diazen-1-ium-1,2-diolates) decompose to form NO in an acid-catalyzed dissociation.[11-13] Of these, (*Z*)-1-[*N*-(2-aminoethyl)-*N*-(2-ammonioethyl)amino]diazen-1-ium-1,2-diolate (DETA/NO) offers the advantage of a long half-life in solution (56 hr at 25 ℃) relative to other NO -donating compounds.[12, 14, 15]

NO has been detected using a range of both direct and indirect techniques.[12, 16, 17] For complex matrices, electrochemistry offers the advantage of direct detection of NO oxidation, allowing NO detection as it is released from biological sources such as cells in tissue slices. Electrochemical detection in biological matrices can be hindered by the presence of multiple electrochemically active species, but selectivity of the detection can be improved through electrode modifications, including electropolymerization to form polymer membranes on electrode surfaces.[18] Many studies have used electrochemical techniques to detect NO,[11, 18-22] though a limited number have employed DETA/NO as the donating compound.[23, 24] The use of DETA/NO as a donor for electrochemical NO detection can be advantageous as the long half-life of DETA/NO provides easily controllable experimental conditions by generating a more constant NO concentration relative to other donors. Electrochemical methods can also provide multiplexed analyte detection with spatial resolution by arranging electrodes in an array.

One advantage of microelectrodes made using modern microfabrication methods is the ability to create arrays that provide spatial resolution. One method to fabricate electrode arrays uses Silicon Metal Oxide Semiconductor (MOS) processes standard to the modern semiconductor industry. Silicon MOS microchips incorporating Complementary Metal Oxide Semiconductor (CMOS) circuits have been used for a wide range of electrochemical sensor applications including measuring neurotransmitter release from chromaffin cells,[25] constructing

portable cell-based biosensors,[26] and development of a multiplexed electrochemical biosensor using a label-free, DNA hybridization-based sensor.[27] Silicon MOS technology has been employed to fabricate high-density electrode arrays,[28] allowing electrochemical detection with high spatiotemporal resolution. The density of the electrode array determines the spatial resolution capabilities of the CMOS chip, and on-board electronics can be incorporated to form expanded biosensor systems to allow simultaneous monitoring at each electrode to provide temporal resolution.[25, 29] These advantages make the silicon-based electrode arrays ideal as a spatiotemporal biosensor for directly monitoring chemical release from cells in tissue slices or cells in dissociated cultures.

In this study, analysis of NO released from DETA/NO using silicon-based microelectrodes in a microfluidic flow system is reported as a first step towards high resolution *in vitro* and *in vivo* monitoring. Potential interfering species were studied using voltammetry, and an electrochemical cleaning method is reported that minimizes the effect of electrode fouling. The detection of NO from DETA/NO by flow injection analysis resulted in a 94±1% signal loss over 10 sequential injections when no cleaning method was used. Cleaning the electrodes prior to each injection reduced this to a 17±13% signal loss over 10 sequential injections. The sensor response was linear for NO detection from 90 nM to 1.0 µM (R^2=0.9987), spanning the reported cellular concentration range.[30, 31]

Experimental

Materials and instrumentation

All chemicals were at least of ACS grade and were used as received without further purification. SU-8 2075 photoresist was obtained from MicroChem (Westborough, MA). Sylgard 184 poly(dimethylsiloxane) (PDMS) oligomer and cross-linker were purchased from Dow Corning (Midland, MI). Hexamethyldisilazane (HMDS), diethylenetriamine (DETA), Tween-20,

HCl, KCl, Na_2HPO_4, and KH_2PO_4 were obtained from Sigma-Aldrich (St. Louis, MO). $NaNO_2$ was purchased from Fisher (Fair Lawn, NJ), and NaCl was purchased from Macron (Avantor, Center Valley, PA). All solutions were prepared using 18.2 MΩ·cm water from a MilliPore (Billerica, MA) Milli-Q system. Phosphate buffered saline (PBS) was prepared from 8.00 g NaCl, 0.20 g KCl, 1.44 g Na_2HPO_4, 0.24 g KH_2PO_4 in 1 L of water, and the pH was adjusted to 7.4 with HCl. All electrochemical experiments were performed using an eDAQ Picostat and e-corder 1621, with eDAQ EChem v2.1 software for voltammetry and eDAQ Chart v5.5.8 for amperometry (eDAQ, Denistone East, Australia). Chemiluminescence experiments were performed using a GE 280i Nitric Oxide Analyzer (GE Analytical Instruments, Boulder, CO, USA).

The microelectrodes were produced by Avago Technologies (Fort Collins, CO) using silicon-based MOS technology and were arranged into 21 groups as previously described.[32] A probe station (Micromanipulator Inc., Carson City, NV) was used to make electrical contact with the silicon microelectrode chip. The probe station was surrounded by a copper faraday cage to reduce electrical noise. Fluid control was accomplished using a NE-1000 Single Syringe Pump (New Era Pump Systems, Farmingdale, NY).

Design and fabrication of microfluidic device

A microfluidic manifold was created using a combination of soft lithography, laser cutting, and 3D printing. The design of the microfluidic manifold and silicon microelectrode chip is shown in Figure 4.1. Figure 4.1A shows a schematic of the four-layered device used to house the silicon microelectrode chip (Figure 4.1B). A microfluidic flow channel was fabricated using standard photolithography and soft lithography techniques.[33, 34] SU-8 2075 photoresist was spin coated onto a 10-cm diameter silicon wafer (Silicon Inc., Boise, ID) to give a final feature height of 174 µm as measured by a ZeScope optical profilometer (Zygo, Middlefield, CT). UV exposure was performed with a photomask (CAD/Art Services, Inc., Bandon, OR) to generate a mold for a

fluidic channel with dimensions 1.5 mm × 20 mm. The mold was coated with HMDS and baked at 115 ºC for 15 min. Standard soft lithography was performed using a degassed 10:1 mixture of PDMS oligomer and cross-linker to generate microfluidic channels. Inlet and outlet ports were cut using 1.5-mm diameter biopsy punches (Robbins Instruments, Inc., Chatham, NJ).

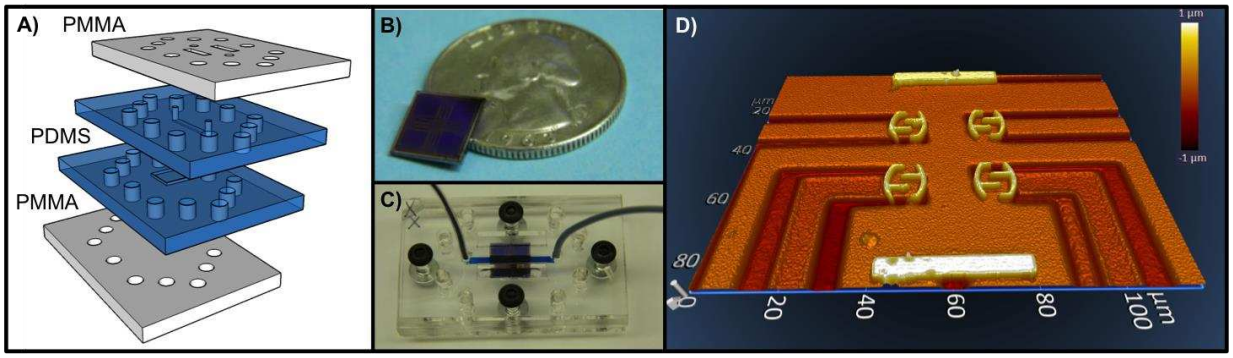

Figure 4.1: Microfluidic setup for the microelectrode chip. **A)** Schematic of device layers and assembly. The bottom and top are PMMA with holes for assembly and access to chip contact pads. The PDMS layers serve to house the microelectrode chip and provide a fluidic interface with the microelectrodes. **B)** 1 cm × 1 cm silicon microelectrode chip, with quarter for size reference. **C)** Assembled device containing the chip. Blue dye is added to the channel for visualization. **D)** One set of microelectrodes on the chip imaged by optical profilometry. The sensor is composed of eight interdigitated working electrodes, a reference electrode at the top, and an auxiliary electrode at the bottom. Scale in z-dimension ranges from -1 µm to 1 µm.

The bottom PDMS layer of the device was fabricated by gluing a microelectrode chip onto a glass slide, coating it with HMDS and baking at 115 ºC for 15 min, and pouring 10:1 PDMS over the chip. The PDMS was used to house a microelectrode chip under the microfluidic channel. Outer plates were cut from 1/8-inch poly(methylmethacrylate) (PMMA) (Fort Collins Plastics, CO) using a laser engraving system (30 W Epilog, Golden, CO) with holes for assembly and access to the contact pads for the microelectrodes. The microelectrode chip was placed in the bottom PDMS layer, and the microfluidic channel was aligned over the electrodes. The device layers were held together using 3-mm diameter, 20-mm long bolts (Figure 4.1C) and placed in a 3D-printed holder (A-101, Lulzbot, Loveland, CO) to interface with the microscope stage. FEP tubing (0.01” ID, 0.0625” OD, IDEX Health and Science, Oak Harbor, WA) was inserted into the PDMS ports for interfacing the chip with fluid. One set of microelectrodes on

the chip was imaged by optical profilometry (Figure 4.1D) and was previously determined to have the optimal electrode geometry among the electrodes on the chip.[32] The set of electrodes used for this work is composed of eight interdigitated working electrodes, a pseudo-reference electrode, and an auxiliary electrode. All microelectrodes on the chip are coated with 700-800 nm Pt with Al routing from the base of the microelectrodes to contacting pads on the edge of the chip. The line width of the microelectrode pattern (Figure 4.1D) is 2 µm.

Preparation of DETA/NO

DETA/NO was prepared using a previously reported method.[14] Briefly, the parent amine, DETA, was reacted in acetonitrile with 80-psi nitric oxide for 24 h. The material was then filtered and rinsed with acetonitrile, placed under vacuum for 5 h to remove remaining solvent, and stored at -20 ºC. Purity was determined using UV-Vis analysis.

Electrochemical characterization using differential pulse voltammetry

Differential pulse voltammetry (DPV) was performed with 10 mM DETA/NO and 10 mM DETA prepared separately in PBS. The microfluidic channel was filled with the analyte solution, and voltammetry was performed without flow using previously reported parameters.[23] The scan range was +0.2 V to +1.0 V (vs. Pt) at a scan rate of 5 mV s^{-1}, with pulse amplitude of 50 mV and pulse width of 70 ms.

Electrochemical cleaning of electrodes

An electrochemical cleaning method was developed and optimized to maintain injection-to-injection signal levels. The cleaning method employed a two-step procedure in PBS flowing at 50 µL min^{-1}. In the first step, +1.2 V was applied for 100 ms. In the second step, two pulses at -1.2 V, each 800 ms long, were applied 400 ms apart (Figure 4.2). This cleaning procedure was used prior to every sample injection in flow injection analysis unless otherwise noted.

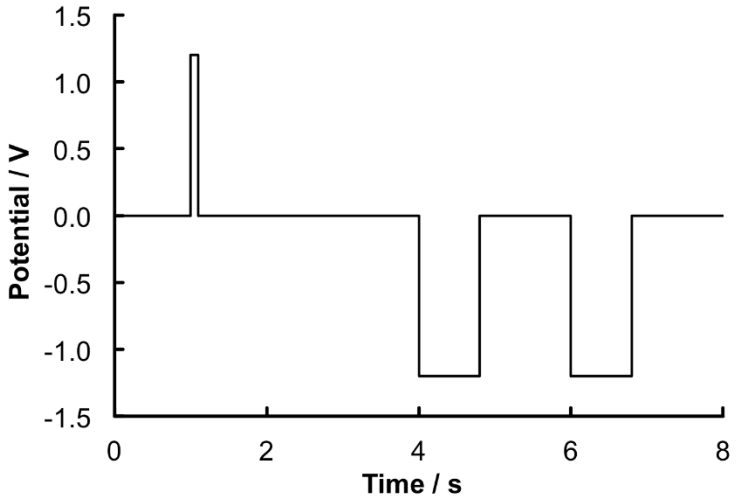

Figure 4.2: Waveform of 2-step cleaning method. The first step is a 100-ms pulse at +1.2 V (vs. Pt). The second step is two 800-ms pulses at -1.2 V that are 1.2 s apart.

Hydrodynamic voltammograms

The effect of applied potential on the output current was studied for DETA/NO and possible interferences DETA and nitrite.[12] Both DETA and nitrite are byproducts generated during the detection of NO from DETA/NO. DETA is generated as DETA/NO decomposes and releases NO, and nitrite is produced after the nitrosonium ion (the oxidation product of NO) reacts with hydroxide in solution.[12] DETA/NO, DETA, and nitrite were prepared separately in PBS at concentrations of 3.5 mM, 5.0 mM, and 10 µM, respectively. Flow injection analysis was performed applying potentials from 0 to +0.8 V (vs. Pt) in 0.1 V increments. Nitrite was only analyzed up to +0.7 V because the nitrite signal became indistinguishable from baseline noise at higher potentials. Samples were injected (n=3) at 10 µL volumes into PBS flowing at 50 µL min^{-1}. Signal was calculated as peak area, and baseline noise was calculated at each potential as the standard deviation of blank injections of PBS (n=6). Error bars represent the standard deviation of replicate (n=3) sample injections.

Sensor response

The response of the sensor to DETA/NO was evaluated using flow injection analysis. DETA/NO samples (0.5-10 mM) in PBS were injected (n=4) at 10 µL volumes into PBS flowing at 50 µL min^{-1} using an applied potential of +0.6 V (vs. Pt).

NO concentration validation by chemiluminescence

DETA/NO solutions were simultaneously monitored using chemiluminescent and electrochemical methods to determine the concentration of NO generated by DETA/NO. A commercial Nitric Oxide Analyzer (NOA) was used for chemiluminescent detection. All measurements were performed at room temperature. NOA calibration was performed using nitrogen (zero gas) and 45 ppm NO/nitrogen. The cell pressure was maintained in the range of 5.5 to 8.5 torr, and the supply pressure was maintained in the range of 4.6 to 6.5 psi. The photomultiplier tube cooler temperature was set at -12 ºC. An empty NOA cell was used to collect baseline measurements for 5 min. Next, 2 mL of PBS was added to the NOA cell. To perform simultaneous electrochemical detection, 200-µL aliquots were removed from the cell and used to fill the 10-µL injection loop for the microelectrode chip. Injections were made into PBS flowing at 50 µL min^{-1} using an applied potential of +0.6 V (vs. Pt). Replicate injections (n=3) were performed from sequential 200-µL aliquots removed from the NOA cell. This process was repeated with DETA/NO solutions (1.0-10 mM) in PBS.

Results and Discussion

Differential pulse voltammetry of DETA/NO

Differential pulse voltammetry (DPV) of DETA/NO and DETA in PBS was performed to determine the optimum oxidation potential for NO detection from DETA/NO without interference from DETA. Oxidation of NO released from DETA/NO occurs at a lower potential than DETA (Figure 4.3), allowing detection of NO from DETA/NO without interference from DETA present in

the solution. DPV of DETA/NO has previously resulted in an oxidation peak at +0.8 V vs. Ag/AgCl,[23] which corresponds to the oxidation potential of NO,[19] indicating that the current observed on the electrodes is a result of NO oxidation rather than oxidation of the DETA/NO molecule. DETA, a byproduct of DETA/NO decomposition, can be oxidized at high potentials due to the presence of amine functional groups. Oxidation of DETA on platinum electrodes has previously been studied using cyclic voltammetry, and the anodic current peak occurred at 1.25 V vs. Ag/AgCl, though the peak potential was observed to shift with different supporting electrolytes.[35] The DPV shown here for DETA reaches the maximum oxidation current at approximately 0.9 V, with negligible signal observed at the 0.6 V used for NO detection.

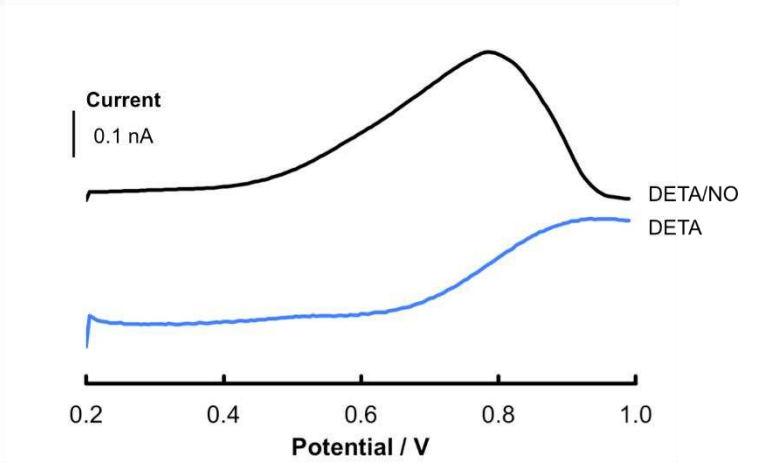

Figure 4.3: Representative scans of 10 mM DETA/NO (—) and 10 mM DETA (—) in PBS pH 7.4. Experimental conditions for differential pulse voltammetry: range +0.2 V to +1.0 V (vs. Pt), pulse amplitude 0.050 V, pulse width 70 ms, scan rate 5 mV s^{-1}. Voltammograms offset for visualization.

Electrode fouling

A loss in electrochemical signal from DETA/NO was observed with subsequent injections in flow injection experiments likely due to oxidative polymerization of DETA on the platinum surface.[35, 36] The DETA generated from the decomposition of DETA/NO contacts the electrode surface, resulting in the formation of a coating that decreases the working area of the electrode. Sets of 10 sequential injections of 12.5, 6.25, and 1.25 mM DETA/NO resulted in a

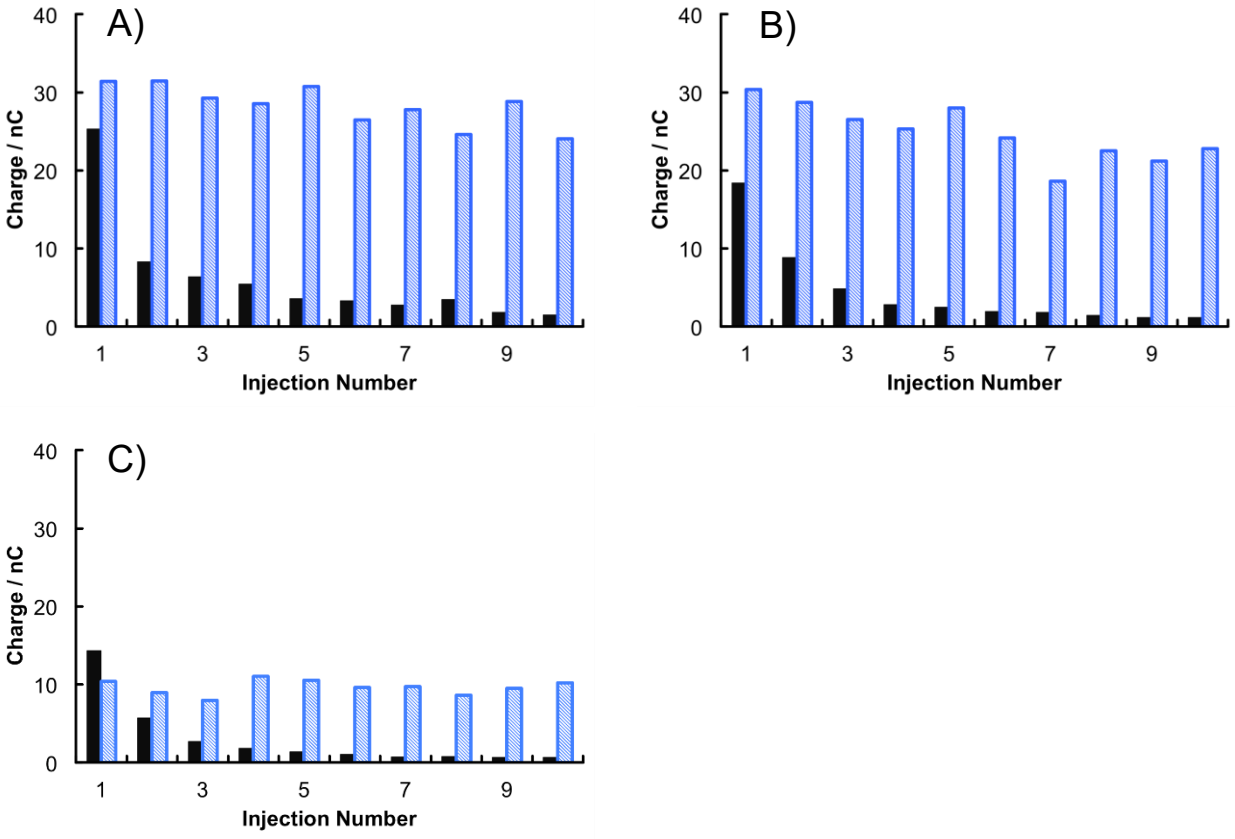

Figure 4.4: Fouling and electrochemical cleaning of electrode surface. Signal plotted as peak area from sequential 10 µL injections of **A)** 12.5 mM DETA/NO (2.5 µM NO) **B)** 6.25 mM DETA/NO (1.25 µM NO) or **C)** 1.25 mM DETA/NO (0.25 µM NO) without (■) and with (▨) electrochemical cleaning step prior to each injection in PBS pH 7.4. Applied potential of 0.6 V (vs. Pt). Flow rate 50 µL min^{-1}.

60±8% loss in signal after one injection, and a 94±1% loss in signal after 10 injections (Figure 4.4).

Multiple methods were investigated to reduce or eliminate electrode fouling. Previous studies have shown that surfactants can minimize fouling of the electrode surface.[37, 38] Injecting a surfactant, 1 mM Tween-20, with the DETA/NO solution to prevent material from accumulating on the electrode surface did not prevent signal degradation (Figure 4.5). Electrochemical cleaning methods have been previously reported to remove material from the electrode surface and maintain constant performance.[39, 40] After investigating multiple waveforms (Figure 4.6), a two-step electrochemical cleaning method was employed prior to every injection. Manica *et al.*[39]

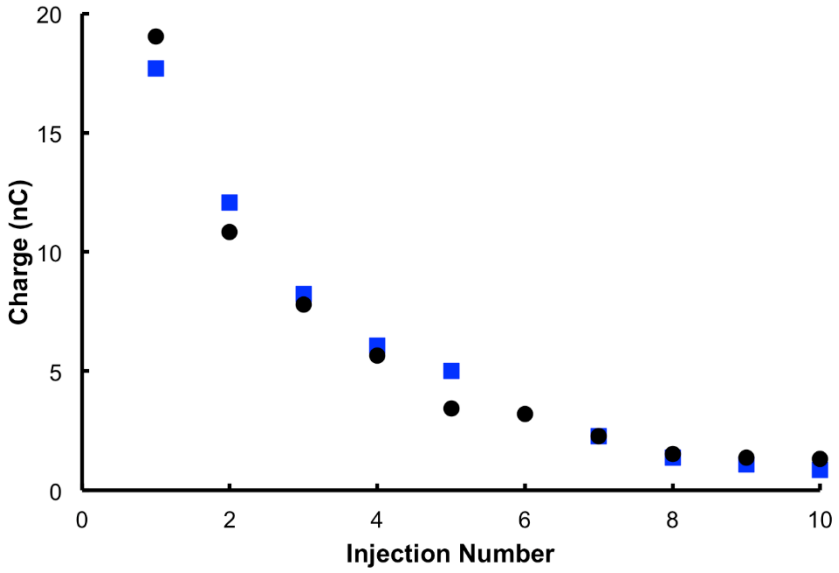

Figure 4.5: Sequential injections of 50 mM DETA/NO without (●) and with (■) alternating 1 mM Tween-20 injections. Flow rate 50 µL min^{-1}. Applied potential of 0.6 V (vs. Pt).

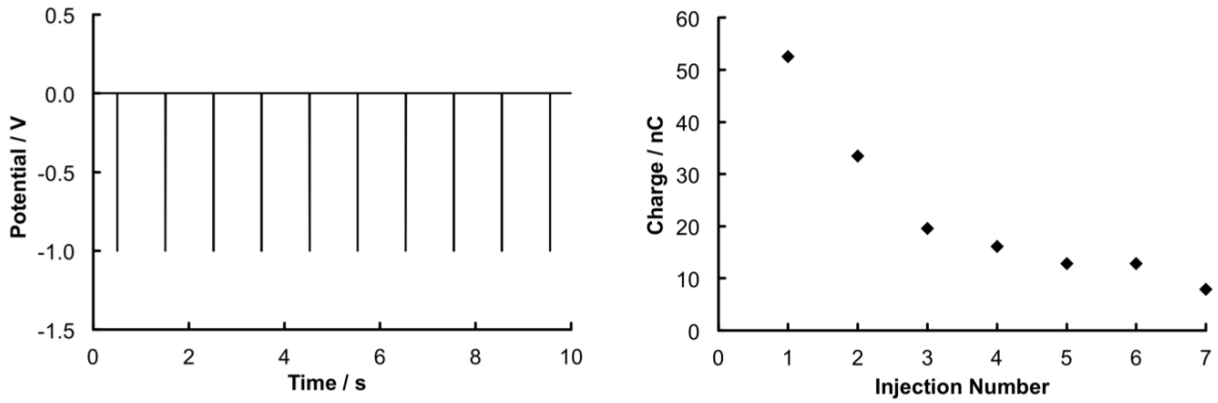

Figure 4.6: Ineffective electrochemical cleaning method. Left panel is waveform of electrochemical cleaning method used in PBS pH 7.4 prior to each injection: 10 pulses 5 ms long at -1 V, 1 s between each pulse. Right panel shows sequential 10 µL injections of 50 mM DETA/NO (10 µM NO) plotted as peak area. Flow rate 50 µL min^{-1}. Applied potential of 0.6 V (vs. Pt).

reported that applying a high oxidation potential to platinum electrodes removes adsorbed organic materials by forming platinum oxide. Applying a subsequent reduction potential will reduce the platinum oxide and regenerate the original electrode surface. In the electrochemical cleaning waveform employed here, +1.2 V was applied for 100 ms followed by two pulses at

−1.2 V, each 800 ms long and 400 ms apart (Figure 4.2). Using the cleaning method prior to every injection reduced the signal loss to 17±13% over 10 injections for 12.5, 6.25, and 1.25 mM DETA/NO with variation in signal across those injections of 11±3% relative standard deviation, indicating that the electrochemical cleaning method was effective at preventing a significant loss in signal (Figure 4.4). Alternative multistep waveforms were investigated utilizing different cleaning potentials, waveform times, and pulse repetitions. These waveforms either did not significantly affect the signal degradation, or were not as effective as the method described above.

Effect of applied potential

Hydrodynamic voltammograms (HDV) of DETA/NO and possible interferences, DETA and nitrite,[12] were next generated to study the effect of applied potential on electrochemical response (Figure 4.7). The response was plotted as the ratio of signal to noise, where the signal was the integrated peak area (n=3), and noise was the standard deviation of the peak area of blank injections (n=6) at each potential. The 10 µM nitrite concentration was chosen as it represents the theoretical maximum concentration present in the DETA/NO solutions at the time of analysis, and nitrite is present at nanomolar to micromolar concentrations *in vivo*.[41, 42] Nitrite generated a negligible signal relative to DETA/NO at all applied potentials. The DETA/NO and DETA responses noticeably increase at 0.6 V and above. The signal was less stable at higher applied potentials, leading to an increase in the variation between injections. An applied oxidation potential of 0.6 V was selected for all subsequent experiments because the DETA/NO signal response is distinguishable from that of DETA, and is more precise than at higher potentials, and the potential is low enough to avoid interfering signals from many naturally occurring species in real samples.

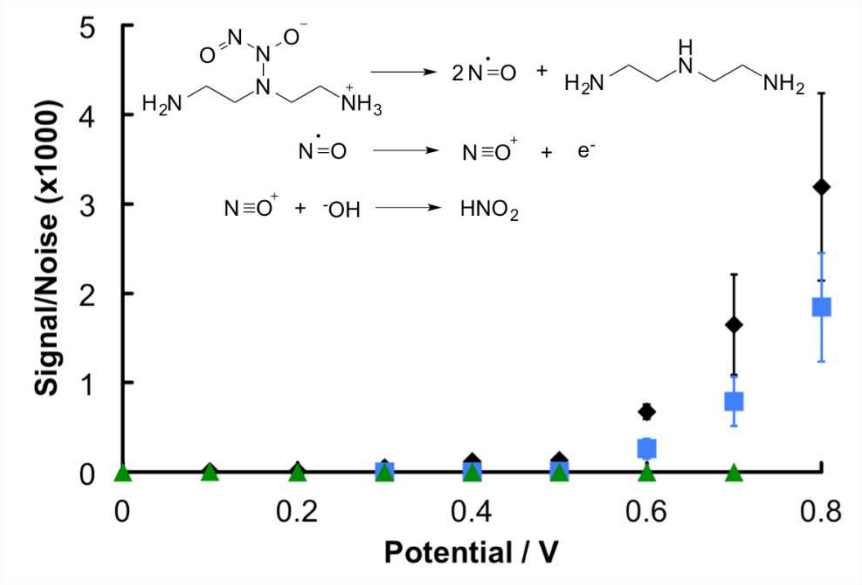

Figure 4.7: Hydrodynamic voltammograms of 3.5 mM DETA/NO (710 nM NO) (◆), 2.5 mM DETA (■), and 10 µM sodium nitrite (▲). Signal is calculated as peak area, and noise is calculated as the standard deviation of the peak area for 6 blank injections at the corresponding potential. Error bars are the standard deviation of replicate10 µL injections (n=3). Species being analyzed are shown in the reactions at the top of the figure. Flow rate 50 µL min^{-1}. Potential applied vs. Pt.

Sensor response

The response of the sensor to NO was evaluated using flow injection analysis of DETA/NO (Figure 4.8). The NO concentration produced from the decomposition of DETA/NO was determined using a commercial NOA. The response from the microelectrodes follows a non-linear trend over the concentration range studied. The response can be approximated as linear (R^2=0.9987) in the range of 90 nM to 1 µM NO, which spans the estimated range of cellular NO concentration,[30, 31] making this electrode system a viable technique for monitoring NO released from cells in dissociated cultures or tissue slices. Deviations from linearity at high concentrations may be a result of decreasing collection efficiency with increasing concentration. Collection efficiency was calculated assuming all NO injected could reach the electrode surface, and resulted in a 3-17% range. The collection efficiency is low because of the size of the working electrode relative to the dimensions of the flow channel, the analysis was performed at a fast flow rate, and the rate of diffusion of DETA/NO to the surface of the electrodes.

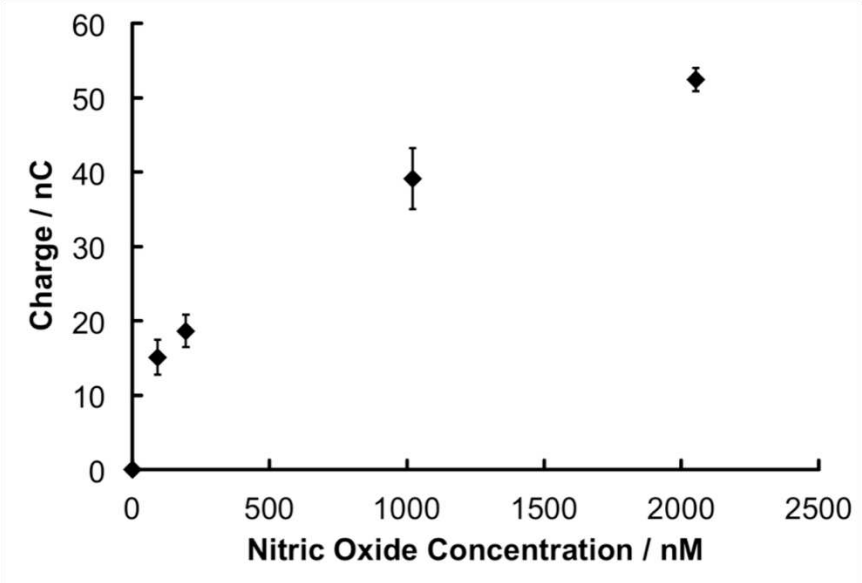

Figure 4.8: Nitric oxide calibration curve from flow injection analysis of DETA/NO in PBS pH 7.4. Signal is plotted as peak area, with error bars representing the standard deviation of replicate 10 µL injections (n=4). Flow rate 50 µL min^{-1}. Applied potential of 0.6 V (vs. Pt).

Conclusions

The work reported here has shown that platinum microelectrodes are a viable technique for monitoring NO. Use of the NO donor DETA/NO results in electrode fouling, but a method for electrochemically cleaning these microelectrodes was demonstrated. The response of the CMOS chip as a function of NO concentration requires further investigation to explain deviations from linearity, but exhibits moderate linearity within the range of cellular NO concentrations. This system can be further developed to generate an array of CMOS electrodes capable of detecting NO release from cells in dissociated cell cultures or tissue slices with high spatiotemporal resolution.

This work is supported in part by National Science Foundation Grant No. GDE-0841259. The authors gratefully acknowledge Sarah M. Lantvit, Jessica M. Joslin, and Bella Neufeld at Colorado State University for synthesizing DETA/NO and use of their NOA. The silicon-based microelectrode chip was manufactured by Avago Technologies. Their technical assistance and generous support for this project are greatly appreciated.

REFERENCES

1. R. M. J. Palmer, A. G. Ferrige and S. Moncada, *Nature*, 1987, **327**, 524-526.

2. M. R. Schaffer, U. Tantry, S. S. Gross, H. L. Wasserkrug and A. Barbul, *Journal of Surgical Research*, 1996, **63**, 237-240.

3. M. B. Witte and A. Barbul, *American Journal of Surgery*, 2002, **183**, 406-412.

4. M. Ziche and L. Morbidelli, *Journal of Neuro-Oncology*, 2000, **50**, 139-148.

5. E. Pipilisynetos, E. Sakkoula and M. E. Maragoudakis, *British Journal of Pharmacology*, 1993, **108**, 855-857.

6. S. H. Snyder, *Science*, 1992, **257**, 494-496.

7. M. A. Degroote and F. C. Fang, *Clinical Infectious Diseases*, 1995, **21**, S162-S165.

8. G. Bicker, *Bioessays*, 2005, **27**, 495-505.

9. S. Bulotta, C. Perrotta, A. Cerullo, C. De Palma, E. Clementi and N. Borgese, *Neurotoxicology*, 2005, **26**, 841-845.

10. A. Contestabile and E. Ciani, *Neurochemistry International*, 2004, **45**, 903-914.

11. T. L. Xu, N. Scafa, L. P. Xu, L. Su, C. Z. Li, S. F. Zhou, Y. Liu and X. J. Zhang, *Electroanalysis*, 2014, **26**, 449-468.

12. L. K. Keefer, R. W. Nims, K. M. Davies and D. A. Wink, *Nitric Oxide, Pt a - Sources and Detection of No; No Synthase*, 1996, **268**, 281-293.

13. J. M. Joslin, S. M. Lantvit and M. M. Reynolds, *Acs Applied Materials & Interfaces*, 2013, **5**, 9285-9294.

14. J. A. Hrabie, J. R. Klose, D. A. Wink and L. K. Keefer, *Journal of Organic Chemistry*, 1993, **58**, 1472-1476.

15. K. M. Davies, D. A. Wink, J. E. Saavedra and L. K. Keefer, *Journal of the American Chemical Society*, 2001, **123**, 5473-5481.

16. O. C. Zafiriou and M. McFarland, *Analytical Chemistry*, 1980, **52**, 1662-1667.

17. F. L. Kiechle and T. Malinski, *American Journal of Clinical Pathology*, 1993, **100**, 567-575.

18. F. Bedioui and N. Villeneuve, *Electroanalysis*, 2003, **15**, 5-18.

19. D. Christodoulou, S. Kudo, J. A. Cook, M. C. Krishna, A. Miles, M. B. Grisham, R. Murugesan, P. C. Ford and D. A. Wink, *Nitric Oxide, Pt a - Sources and Detection of No; No Synthase*, 1996, **268**, 69-83.

20. C. Amatore, S. Arbault and A. C. W. Koh, *Analytical Chemistry*, 2010, **82**, 1411-1419.

21. K. Shibuki, *Neuroscience Research*, 1990, **9**, 69-76.

22. C. Calas-Blanchard, G. Catanante and T. Noguer, *Electroanalysis*, 2014, **26**, 1277-1286.

23. V. C. Diculescu, R. M. Barbosa and A. M. O. Brett, *Analytical Letters*, 2005, **38**, 2525-2540.

24. N. R. Ferreira, A. Ledo, J. G. Frade, G. A. Gerhardt, J. Laranjinha and R. M. Barbosa, *Analytica Chimica Acta*, 2005, **535**, 1-7.

25. B. N. Kim, A. D. Herbst, S. J. Kim, B. A. Minch and M. Lindau, *Biosensors & Bioelectronics*, 2013, **41**, 736-744.

26. B. D. DeBusschere and G. T. A. Kovacs, *Biosensors & Bioelectronics*, 2001, **16**, 543-556.

27. J. Rothe, M. K. Lewandowska, F. Heer, O. Frey and A. Hierlemann, *Journal of Micromechanics and Microengineering*, 2011, **21**, 10.

28. K. M. Roth, K. Peyvan, K. R. Schwarzkopf and A. Ghindilis, *Electroanalysis*, 2006, **18**, 1982-1988.

29. S. Ayers, K. D. Gillis, M. Lindau and B. A. Minch, *Ieee Transactions on Circuits and Systems I-Regular Papers*, 2007, **54**, 736-744.

30. M. B. Grisham, D. Jourd'Heuil and D. A. Wink, *American Journal of Physiology-Gastrointestinal and Liver Physiology*, 1999, **276**, G315-G321.

31. D. A. Wink and J. B. Mitchell, *Free Radical Biology and Medicine*, 1998, **25**, 434-456.

32. W. Pettine, M. Jibson, T. Chen, S. Tobet, P. Nikkel and C. S. Henry, *Ieee Sensors Journal*, 2012, **12**, 1187-1192.

33. D. C. Duffy, J. C. McDonald, O. J. A. Schueller and G. M. Whitesides, *Analytical Chemistry*, 1998, **70**, 4974-4984.

34. Y. Sameenoi, M. M. Mensack, K. Boonsong, R. Ewing, W. Dungchai, O. Chailapakul, D. M. Cropek and C. S. Henry, *Analyst*, 2011, **136**, 3177-3184.

35. L. Ouattara, T. Diaco and Y. Bokra, *Bulletin of the Chemical Society of Ethiopia*, 2006, **20**, 269-277.

36. G. Herlem, K. Reybier, A. Trokourey and B. Fahys, *Journal of the Electrochemical Society*, 2000, **147**, 597-601.

37. B. Hoyer and N. Jensen, *Electroanalysis*, 2005, **17**, 2037-2042.

38. B. Hoyer and N. Jensen, *Electrochemistry Communications*, 2006, **8**, 323-328.

39. D. P. Manica, Y. Mitsumori and A. G. Ewing, *Analytical Chemistry*, 2003, **75**, 4572-4577.

40. H. Moller and P. C. Pistorius, *Journal of Electroanalytical Chemistry*, 2004, **570**, 243-255.

41. J. Rodriguez, R. E. Maloney, T. Rassaf, N. S. Bryan and M. Feelisch, *Proceedings of the National Academy of Sciences of the United States of America*, 2003, **100**, 336-341.

42. P. Kleinbongard, A. Dejam, T. Lauer, T. Rassaf, A. Schindler, O. Picker, T. Scheeren, A. Godecke, J. Schrader, R. Schulz, G. Heusch, G. A. Schaub, N. S. Bryan, M. Feelisch and M. Kelm, *Free Radical Biology and Medicine*, 2003, **35**, 790-796.

CHAPTER 5. SPATIOTEMPORAL NOREPINEPHRINE MAPPING USING A HIGH-DENSITY CMOS MICROELECTRODE ARRAY

Introduction

A high-density amperometric electrode array containing 8,192 individually addressable platinum working electrodes with an integrated potentiostat fabricated using Complementary Metal Oxide Semiconductor (CMOS) processes is reported. The array was designed to enable electrochemical imaging of chemical gradients with high spatiotemporal resolution. Electrodes are arranged over a 2 mm × 2 mm surface area into 64 subarrays consisting of 128 individual Pt working electrodes as well as Pt pseudo-reference and auxiliary electrodes. Amperometric measurements of norepinephrine in tissue culture media were used to demonstrate the ability of the array to measure concentration gradients in complex media. Poly(dimethylsiloxane) microfluidics were incorporated to control the chemical concentrations in time and space, and the electrochemical response at each electrode was monitored to generate electrochemical heat maps, demonstrating the array's imaging capabilities. A temporal resolution of 10 ms can be achieved by simultaneously monitoring a single subarray of 128 electrodes. The entire 2 mm × 2 mm area can be electrochemically imaged in 64 seconds by cycling through all subarrays at a rate of 1 Hz per subarray. Monitoring diffusional transport of norepinephrine is used to demonstrate the spatiotemporal resolution capabilities of the system. The data reported here expand the number of biomarkers we have detected using CMOS microelectrode arrays and provides us with the capability to generate quantitative electrochemical images with spatiotemporal resolution. This work was published in *Lab on a Chip*, Issue 20, in 2015. This work was a collaborative effort between John Wydallis, who designed the microfluidics and did the majority of the data collection, Rachel Feeny, who did the data analysis, William Wilson, and Tucker Kern, who both did all of the electronics design and integration.

Molecular gradients are important driving forces in biology, directing phenomena such as chemotaxis,[1-3] cancer metastasis,[4] and cell-to-cell communication.[5-7] These processes occur over multiple length scales, ranging from synaptic gaps in angstroms to entire organs in centimeters, and time periods ranging from milliseconds to minutes. The ability to simultaneously monitor chemical gradients and observe cellular responses to those gradients across multiple length scales can provide a critical foundation for understanding biological phenomena.

Monitoring biological processes driven by molecular gradients requires a system capable of generating images with high spatiotemporal resolution and chemical selectivity. Optical and fluorescence microscopies have long been used to observe molecular gradients in biology. Microscopy techniques are ideal in many respects for monitoring chemical gradients in biological systems with spatial and temporal resolution. Unstained living tissue can be imaged using endogenous fluorophores, such as nicotinamide adenine dinucleotide (NADH) and hemoglobin,[8, 9] avoiding the necessity for exogenous probes. Genetic modification, stains, and probes, including fluorescent proteins, quantum dots, and metal chelates can be used to expand the library of molecules detectable by fluorescence techniques, but many species remain inaccessible or have altered activity when conjugated with fluorescent probes.[10-12] Other techniques such as mass spectrometry can detect a large library of molecules with spatial resolution, though these systems typically lack the temporal resolution required to monitor dynamic changes in concentration gradients, as tissues are no longer viable at the time of analysis.[13, 14]

Electrochemistry can provide an alternative way to create a chemical map or “image” that can augment observations from traditional microscopy by detecting, with spatial and temporal resolution, changes in key signaling molecules that cannot be readily measured using microscopy methods. Electrochemical imaging on a microscopic scale has previously been described in the context of scanning electrochemical microscopy (SECM),[15-17] microfluidic

sampling devices,[18, 19] and microelectrode arrays.[20-24] SECM measures current response from a single electrode rastered over a surface to generate images.[15-17] SECM can provide evidence of chemical release with high spatial resolution but requires physical scanning over the surface and thus has limited temporal resolution. Microelectrode arrays offer improved temporal resolution because the electrodes do not move and multiple electrodes can be operated simultaneously. The Baltes, Hierlemann, and Matsue groups have described micro- and nanoelectrode systems fabricated from Complementary Metal Oxide Semiconductor (CMOS) techniques as analytical tools.[25-30] These reports use high-density electrode systems to map cellular electrical signals with subcellular resolution or use redox cycling to generate electrochemical responses to image chemical distributions. While effective, most electrode array-based imaging applications have used tens of electrodes for cellular or sub-cellular imaging or use larger arrays to define voltage gradients across neuronal networks.[20, 21, 31-33] Arrays with higher electrode density and/or large numbers of electrodes have primarily been employed for impedance or voltage-based sensing and not amperometric detection.[23, 34-38] As a preliminary study of the capabilities of an electrode array to image chemical distributions on the scale of an *ex vivo* tissue slice, the system described here was used to image controlled distributions of norepinephrine as a model neurotransmitter.

The system described here uses a high-density electrode array with an on-board potentiostat to make amperometric measurements across a 2 mm x 2 mm array. The array has a spatial resolution of 30 µm, a temporal resolution of 10 ms per 250 µm x 250 µm subarray region, and contains 8,192 individual Pt microelectrodes in addition to on-board reference and auxiliary electrodes. The array was fabricated using standard commercial Complementary Metal Oxide Semiconductor (CMOS) techniques with an added lift-off step to give the final Pt layer for the working electrodes. The die size fits onto the stage of an upright microscope so that optical and electrochemical images can be obtained simultaneously. Images were obtained for

norepinephrine gradients formed *via* either diffusion or hydrodynamic flow directed using a microfluidic device.

Experimental

Materials and instrumentation

All chemicals were at least of ACS grade and used as received without additional purification. SU-8 2075 photoresist was obtained from MicroChem (Westborough, MA). Hexamethyldisilazane (HMDS) and (±)-norepinephrine (+)-bitartrate salt were purchased from Sigma-Aldrich (St. Louis, MO). Sylgard 184 poly(dimethylsiloxane) (PDMS) oligomer and cross-linker were obtained from Dow Corning (Midland, MI). Neurobasal-A media without phenol red was purchased from Life Technologies Corporation (Carlsbad, CA) and was used in all electrochemical experiments to demonstrate compatibility with solutions required for sustaining *in vitro* cell and tissue culture. Dyes (FD&C Red #40 and Blue #1) used for solution visualization were purchased from Kroger (Cincinnati, OH). External power supplies (HP E3630A and E3631A Triple Output DC Power Supplies, Hewlett Packard, Palo Alto, CA) were used to power the system containing the electrode array chip. Optical images and videos were collected using a commercial smartphone (Apple Inc., Cupertino, CA) and a fluorescent magnifier light (LumaPro, W. W. Grainger, Lake Forest, IL). Chip control and data collection were achieved using ADLINK DAQe-2200 data acquisition boards. Data post-processing including electrochemical heat map generation was performed using a suite of MATLAB functions (32 bit and 64 bit, Mathworks, Inc., Natick, MA). The electrode array was imaged using a ZeScope optical profilometer (Zygo, Middlefield, CT) and a JSM-6500F scanning electron microscope (JEOL USA Inc., Peabody, MA).

Electrode array design, fabrication, and operation

Chip fabrication and operation. Figure 5.1 shows optical profilometry and scanning electron microscopy (SEM) images of individual electrodes, a single subarray, and the entire array as well as a photograph of the system after mounting in its ceramic packaging. The electrode array chip was designed in a 0.5-µm 4-layer metal CMOS process. The top layer metal was used for patterning Pt electrodes. The metal layers 1-3 provided necessary routing for the chip.

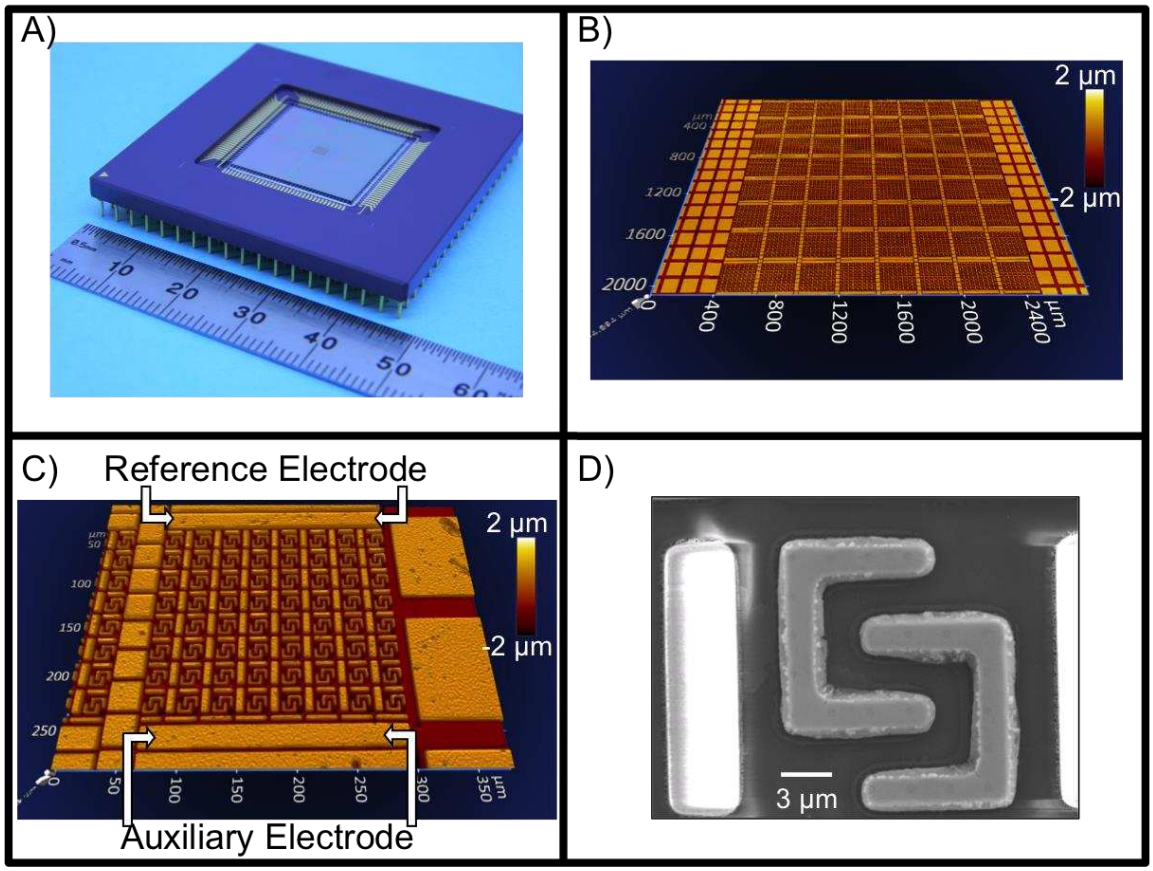

Figure 5.1: Images of the high-density electrode array. **A)** Photograph of CMOS chip containing electrodes and on-chip potentiostat. **B)** Optical profilometry image of entire array showing 64 subarrays. **C)** Optical profilometry image of a single subarray comprised of 128 working electrodes and shared auxiliary and pseudo-reference electrodes. **D)** SEM image of two interdigitated platinum working electrodes 12.5 µm long on the y-axis.

Manufacturing of the electrode array chip was performed by Avago Technologies on 8-inch wafers using Avago's fabrication facility in Fort Collins, Colorado. The die size is 1.9×1.9 cm^2. The process of forming the Pt electrode in the electrode array chip is as follows:

1. The process starts with a lightly doped p-type silicon substrate. (The CMOS process used for the chip is an n-well CMOS process);
2. All on-chip electronic components (logic gates, amplifiers, etc.), including metal routing patterns to connect electrodes on Metal 4 to the I/O pads, are manufactured up to Metal 3 using the standard CMOS manufacturing process;
3. Chemical and mechanical polishing (CMP) is performed to make the post-Metal-3 surface planar;
4. SiO_2 and Si_3N_4 layers are deposited on the surface of the chip. Si_3N_4 acts as the passivation layer;
5. Chemical and mechanical polishing (CMP) is performed to make the surface planar;
6. Etching is performed to allow the formation of contacts from the passivation layer surface to the Metal 3 routing pattern at the base of the electrodes formed in step 2;
7. A Ti/TiN barrier layer is deposited inside the contact well to provide a buffering layer for tungsten;
8. Tungsten is deposited to fill the contact well to form the vertical contact column to the raised electrode on the passivation layer surface;
9. The base of the electrodes at the passivation layer surface using a thin platinum diffusion barrier on the order of tens of nm. This diffusion layer makes electrical contact to the tungsten plug as well as acting as the base layer for Au/Pt tip of the electrodes;
10. The body of the electrode tips on the chip surface is formed using Au with Pt coating surrounding the tips. The height of the tips from the chip surface is 1.5 µm. The electrodes were intentionally designed to rise above the surface to allow better contact between the electrode and tissue slices that will ultimately be studied.

Figure 5.2 shows the cross section of the electrodes manufactured using the steps described above (not to scale). Figure 5.3 shows the top view of one pair of working electrodes with dimensions clearly marked. The on-chip potentiostat has a voltage regulating error of no more

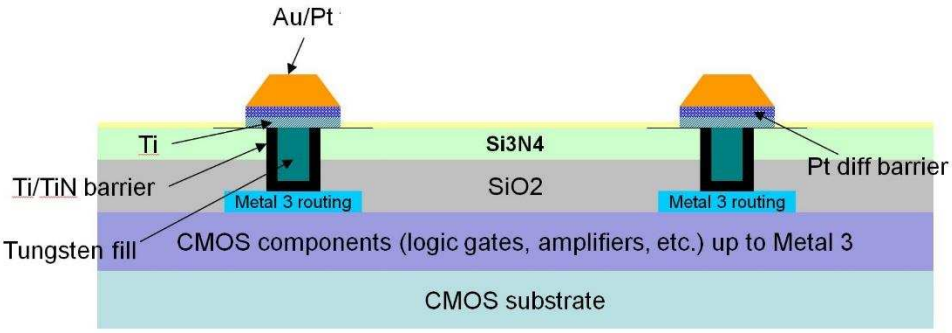

Figure 5.2: Cross section of the Pt electrodes (not to scale).

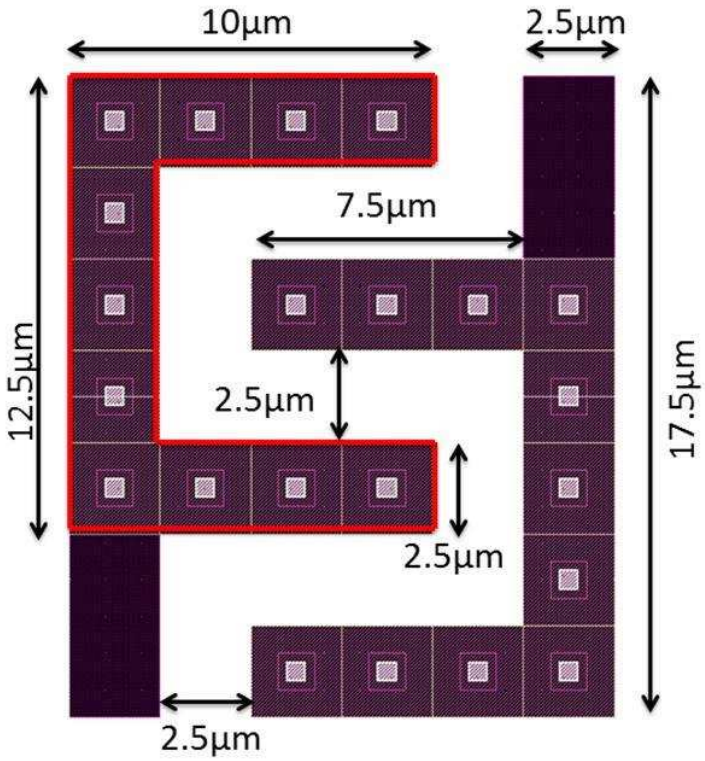

Figure 5.3: A pair of working electrodes designed with an “F” shape.

than 8 mV in amperometry mode. In voltammetry mode, it is capable of providing up to 10 kV s^{-1} scan rate with the same voltage regulating error. The on-chip control logic also provides flexibility of connecting any electrodes in a subarray directly to the chip I/O pins to allow direct access of electrodes using external potentiostats.

A 96-input data acquisition card (ADLINK DAQe-2200 series) was used, allowing cycling through 96 of the 128 electrodes on each of the 64 subarrays at set intervals to provide imaging results. In the experiments described here, the data were collected from the array by monitoring individual subarrays and cycling through each subarray vertically, starting in the upper-right corner of the array and ending in the bottom-left corner. The subarray switching parameters are definable by the user in custom-designed MATLAB functions through a windows-based graphical user interface. The current response at individual electrodes was converted to color intensity and plotted to generate electrochemical heat maps using a custom MATLAB program. Table 5.1 details the electrical specifications of the microchip.

Table 5.1: CMOS chip specifications.

Specification	**Value**
Electrode Pitch	30 µm
Subarray Dimensions	250 µm × 250 µm (128 electrodes)
Array Dimensions	2 mm × 2 mm (8192 electrodes)
Maximum Experimental Data Collection Rate (Single Subarray)	100 Hz
Maximum Experimental Data Collection Rate (Entire Array)	0.0156 Hz

*Electrode array format***.** All 8,192 working electrodes are located at the center of the chip in a 2 mm × 2 mm area. Electrodes were grouped in 64 subarrays each with 128 electrodes. Each subarray has its own Pt pseudo-reference electrode (RE) and counter electrode (CE). The design of the working electrodes was previously optimized and used for biomarker detection in a microfluidic manifold.[39, 40] Figure 5.4 shows the arrangement of 128 working electrodes and RE

and CE in each subarray. The electrode array chip is housed in a 280-pin ceramic cavity-up PGA package. There are 128 I/O pads on the ceramic PGA package dedicated to the

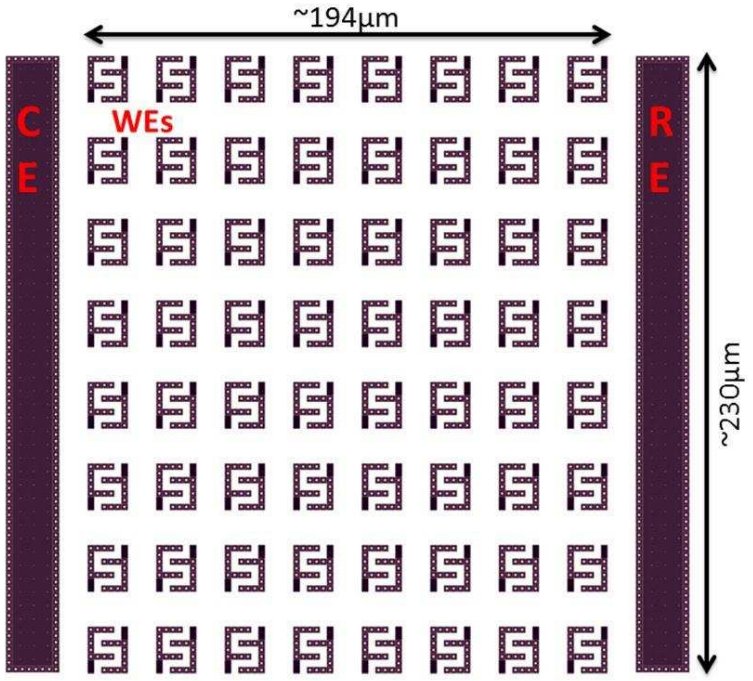

Figure 5.4: A single subarray of 128 working electrodes, one pseudo-reference electrode, and one auxiliary electrode.

electrodes in subarrays. All 128 electrodes in a given subarray can be selected and connected to the I/O pads through an on-chip 64-to-1 multiplexer. Finally, the electrodes were connected to on-board logic and a potentiostat circuit capable of addressing 128 electrodes in a subarray as well as switching between subarrays. The on-chip circuits consist of an 8,192-electrode array, electrode subarray selection logic, and a potentiostat circuit for the on-chip RE, CE, and WEs as shown in Figure 5.5. Each electrode in each subarray is connected to a switch that will be turned on or off by a 3:8 decoder. The switches are then connected out to one of the 128 transimpedance amplifiers (TIAs) in the on-board read-channels, as outlined in Figure 5.6. Each of the electrode pairs in the figure represents one 128-electrode subarray, of which there are 64 total. Although there are separate switches for each electrode in a pair, both the vertical and

horizontal switches are controlled by the same decoder so that all 128 electrodes of a single subarray will be on at the same time.

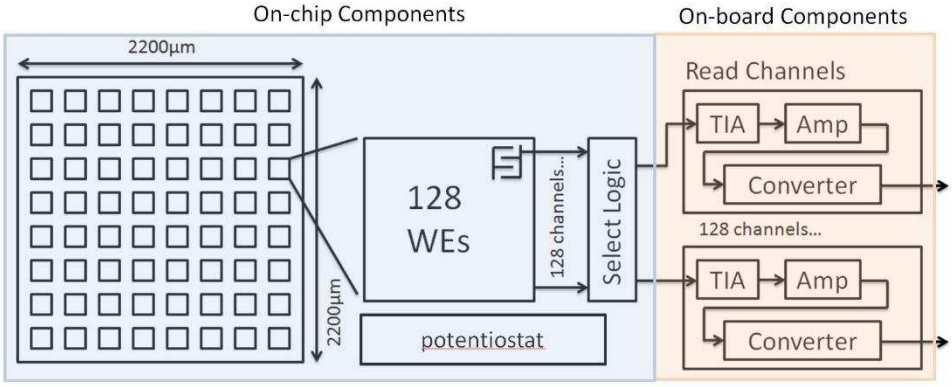

Figure 5.5: On-chip components and how they connect through select logic to 128 on-board read-channels.

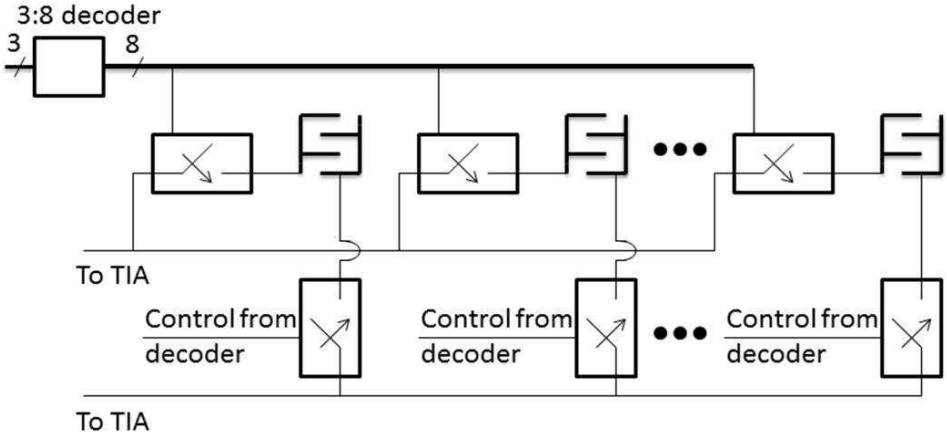

Figure 5.6: Control logic for the electrode subarrays.

Although each subarray has its own reference and auxiliary electrode, only one potentiostat was needed for the entire design. The main goal of the potentiostat is to maintain a constant potential between the working electrodes and a RE while supplying current to a CE. A bias voltage is applied to the RE and the corresponding induced current will describe the concentration of the chemical present at the working electrode. Each of the auxiliary and reference electrodes found in the subarrays is connected together so that only one potentiostat is required to control the entire array. The potentiostat is designed to operate up to 10,000 V s^{-1}

for cyclic voltammetry and in the range of -1 V to +1 V for amperometry. The single op-amp structure used for the potentiostat is based on our proposed self-biased inverter based design[41] and is shown in Figure 5.7.

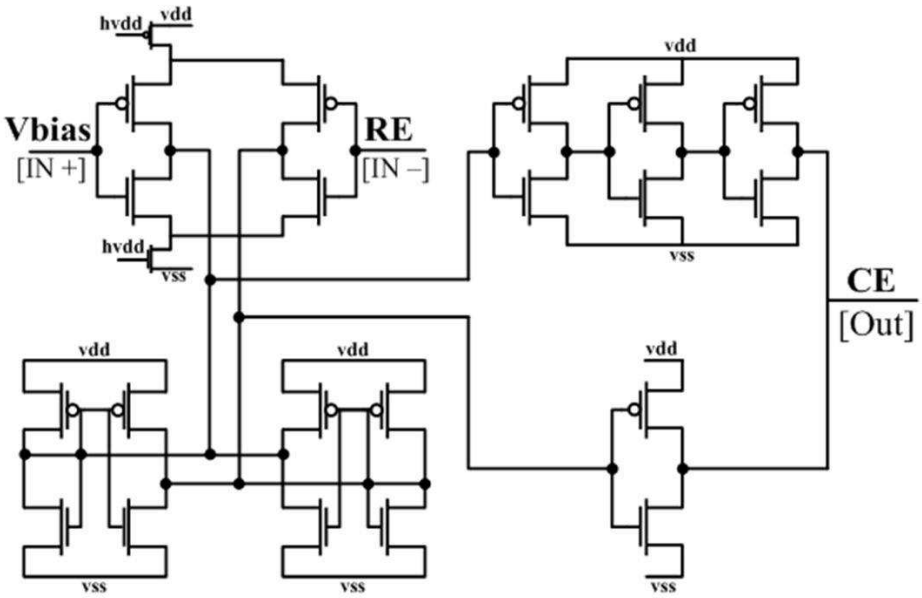

Figure 5.7: A self-biased inverter based potentiostat circuit.

The outputs from 128 selected electrodes are connected to 128 read-channels on a circuit board. Each read-channel on the circuit board consists of a transimpedance amplifier (TIA) and a main amplifier. The transimpedance amplifier has a gain of 10 MΩ. The purpose of the main amplifier is interfacing with the analog-digital converter used. The main amplifier has a gain of 2. Figure 5.8 shows the organization of the board-level components. The block in the middle is the custom electrode array chip. The read-channels receive the current and voltage signals from the 280-pin package on the board for amperometric and voltammetric operations, respectively.

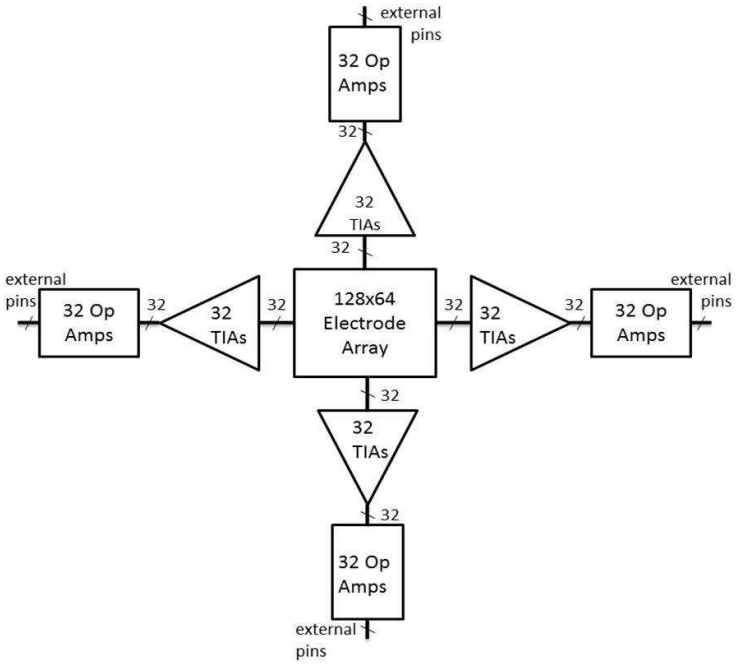

Figure 5.8: Main board-level components.

The circuit board is manufactured by Advanced Circuits Inc. with 4 layers of signals routing. In addition to 128 read-channels, the circuit board also contains voltage regulators, control logic for the custom electrode array chip and for the data acquisition board on the host computer. Figure 5.9 shows the circuit board for the 8,192-electrode array system. The 128-channel output from the circuit board is sampled by a data acquisition board through a host PC. The data acquisition board that works with the electrode array circuit board is an ADLink 2200 series 64-/96-CH high performance multi-function data acquisition card. Data acquisition from 128 data sources is triggered by the electrode array circuit board. A suite of Matlab functions have been developed to provide interface between the electrode array chip, the on-board read-channels, and the data acquisition board inside the host PC. Custom signal processing functions were also developed in MATLAB and C++ for generating electrochemical images from the raw data acquired by the system.

Figure 5.9: Circuit board with the electrode array chip in the middle and other supporting circuits around it.

For all experiments described here, a 100 Hz data collection rate was used for an active subarray, and subarrays were cycled at a switching rate of 1 Hz when applicable. The on-chip potentiostat was used to apply an oxidation potential of +0.6 V (vs. Pt) for norepinephrine detection and a custom MATLAB script was used to generate electrochemical heat map images and videos for all experiments.

Fabrication of microfluidic devices

Microfluidics were interfaced with the chip using a combination of soft lithography[42, 43] and laser cutting.[44, 45] Wafers and molds were coated with HMDS and baked at 115 ºC for 15 min for easy removal of the PDMS. All microfluidics were fabricated using two layers of PDMS. The bottom layer, which interfaces directly with the CMOS chip, was a 2-mm thick layer of a degassed 30:1 mixture of PDMS oligomer and cross-linker. This PDMS formulation gave higher adhesion to the CMOS chip, allowing for higher flow rates without leakage. After curing the first layer, a 3-mm thick layer of a degassed 10:1 mixture of PDMS oligomer and cross-linker was poured directly on top of the first layer and cured at 80 ºC. This second layer was included to improve the structural integrity of the fluidics and to prevent adhesion to the poly(methylmethacrylate) (PMMA) compression plate described below. Wells used to contain

samples over the electrode array were fabricated by making these two layers on a pristine silicon wafer (Silicon Inc., Boise, ID). A biopsy punch (Robbins Instruments, Inc., Chatham, NJ) was used to create a 10-mm diameter well in the PDMS.

A Y-shaped microfluidic flow channel was fabricated using soft lithography.[42, 43] SU-8 2075 was spin coated onto a 10-cm diameter silicon wafer to achieve a final feature height of 104 ± 1 µm (n = 7) as measured by optical profilometry. A Y-shaped microfluidic channel 2.5 mm wide and 7 mm long, with entrance channels 1.75 mm wide and 4.5 mm long was used. PDMS was poured and cured as described above to make the device. A biopsy punch was used to create 1-mm diameter inlets and outlets to interface the device with vinyl PVC tubing (1/32" ID, 3/32" OD, Thermo Fisher Scientific, Waltham, MA), stainless steel connectors (Loctite, Henkel Corporation, Westlake, OH), and NE-1000 Single Syringe Pumps (New Era Pump Systems, Farmingdale, NY) for fluid control.

A second microfluidic device was fabricated to allow fluid transfer across the array *via* head pressure and consisted of two reservoirs connected by a straight channel. Standard photolithography was performed using SU-8 2075 to generate a mold for a microfluidic channel with dimensions 82 µm × 2.5 mm × 6.0 mm. The mold was treated with HMDS, and two layers of PDMS were created as described above. A 5-mm diameter reservoir was punched at both channel ends using a biopsy punch.

A poly(methylmethacrylate) (PMMA) compression manifold was used to prevent fluid leaks from the Y-channel at high flow rates by applying additional pressure to the PDMS on the CMOS chip surface. The plate was cut from 1/8-in thick PMMA (Fort Collins Plastics, CO) using a CO_2 laser engraving system (30 W Epilog, Golden, CO). The plate contained 3-mm diameter holes for access to the inlets and outlet of the channel, a space for the arm of the socket used to interface the silicon chip with the printed circuit board (Textool™ Burn-In Grid ZIP Socket, 3M, Saint Paul, MN), and holes to attach the plate to the printed circuit board. Nylon screws (1.5 in)

and wing nuts were used to hold the plate in place and increase the amount of pressure applied to the PDMS. An image of the setup can be seen in Figure 5.10.

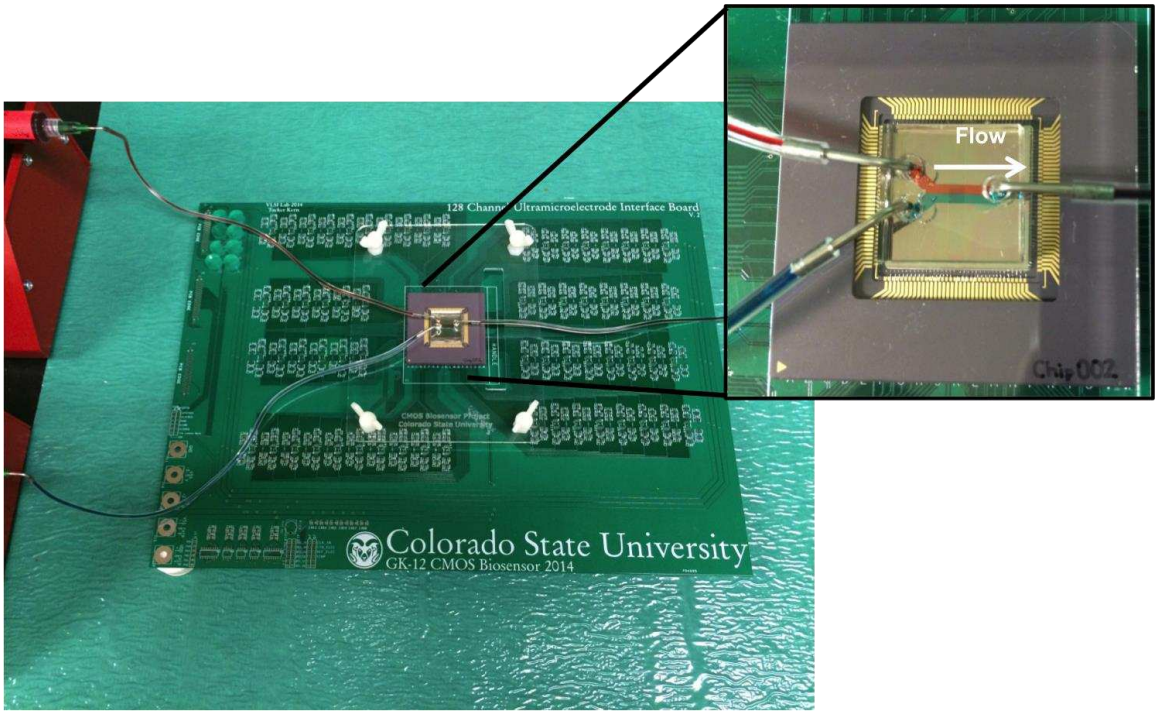

Figure 5.10: Setup for microfluidic experiments. The syringe pumps at the left pump two different fluids into the Y-shaped microfluidic channel positioned across the chip (inset image). The chip is connected to the PCB, and the microfluidics are compressed onto the chip using a custom-cut PMMA plate with nylon screws.

Diffusion of norepinephrine across a subarray

Electrochemical detection of norepinephrine with spatial and temporal resolution was studied using a single subarray (96 of 128 electrodes). A 10-mm diameter well was placed on the CMOS chip with the array positioned in the lower right region of the well and 200 µL of media was added to well. MATLAB was used to monitor a single subarray throughout the entire experiment. A 10-µL drop of 100 mM norepinephrine in media was added to the top left region of the well, resulting in a final norepinephrine concentration of 4.8 mM after complete diffusion. The current resulting from the oxidation of norepinephrine was collected on the subarray as the solution travelled throughout the well.

Norepinephrine diffusion across array

The spatial and temporal resolution of the array was next studied by monitoring slow fluid transport controlled by head pressure and diffusion. Media and a norepinephrine solution were prepared with dye for visualization. Blue media was used as a baseline and red media was used to indicate the presence of norepinephrine in the media. The flow of media containing norepinephrine was controlled by the relative head pressure in each reservoir. First, 20 µL of media was added to one reservoir to fill the flow channel with media and establish a baseline. Next, 19 µL of 10 mM norepinephrine was added to the second reservoir, and additional 0.5-µL aliquots of 10 mM norepinephrine were added to the second reservoir until the head pressure increased enough to begin to push the norepinephrine into the connecting channel. Head pressure and diffusion then slowly drove norepinephrine across the array and the resulting current was monitored across the array.

Bimodal distribution of norepinephrine across the array

Electrochemical images of controlled chemical distributions were generated by using a Y-shaped microfluidic channel on the CMOS chip to produce a bimodal gradient of norepinephrine across the array. Media and a norepinephrine solution were prepared with dyes as described above. Fluid control was achieved using two syringe pumps. Baseline signals were collected by flowing media across the array at 100 µL min^{-1}. The syringe pump containing the 10 mM norepinephrine solution was then started at 50 µL min^{-1} while the media was simultaneously decreased to a flow rate of 50 µL min^{-1} to maintain a total flow rate of 100 µL min^{-1} generating a bimodal norepinephrine gradient across the array.

A similar experiment was carried out to position the bimodal gradient over different portions of the array. After flowing media at 100 µL min^{-1} to establish a baseline, the flow rates were adjusted to have the 10 mM norepinephrine solution sequentially contribute to 25, 50, 75, and 100% of the total 100 µL min^{-1} flow rate, cycling through the entire array at least once

between each change in flow rate. Video of the flow was taken using a commercial smartphone to compare to the electrochemical heat maps.

Results and Discussion

The high-density Pt microelectrode array described here was designed as a platform for imaging chemical distributions with high spatiotemporal resolution. Unlike previous examples of electrode-based imaging arrays, amperometric current was measured (as opposed to impedance) using an on-chip potentiostat. Electrode spacing in a high-density array determines the spatial resolution of the system and on-board electronics control the temporal resolution. Chemical distributions were controlled across the array using simple microfluidics to generate electrochemical images for demonstration of the spatiotemporal capabilities of the array. Variability among electrodes has been observed, and experiments are underway to understand the cause of variation in sensitivity. Slight differences in the electrodes, such as raised edges or small changes in surface area may be resulting in significant differences in signal. The short-term solution employed here is the use of standards, and a thorough investigation of electrode variability will be performed prior to using this platform for quantitative spatiotemporal imaging of chemical release from live tissue.

Diffusion of norepinephrine across a subarray

A norepinephrine gradient was generated by diffusion across the CMOS array to study the temporal resolution of a single subarray. Current was monitored at 96 electrodes on the subarray and was plotted as a function of time for three representative electrodes in different locations on the subarray (Figure 5.11). An electrochemical video of the results can be viewed at http://sites.chem.colostate.edu/henrylab/cmosvideo1.html.

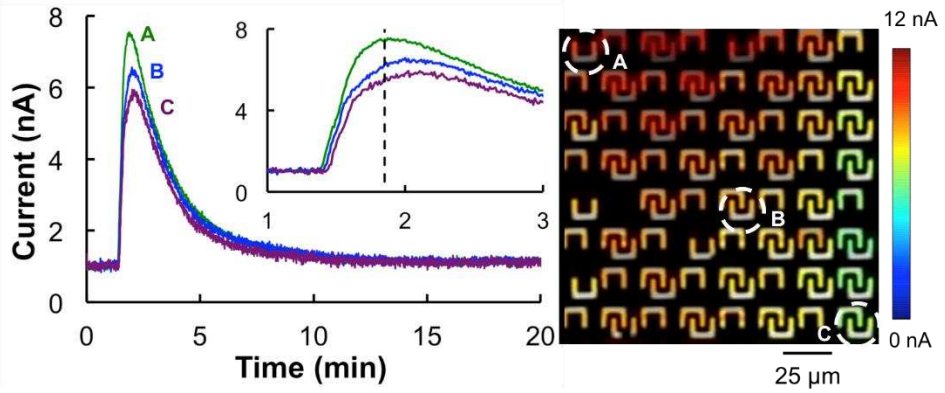

Figure 5.11: Diffusion of norepinephrine across a subarray. **Left)** Amperograms correspond to electrodes indicated on the heat map on the right. Electrodes closest to the source of the norepinephrine reach the highest signal, and all electrodes end at the same signal after the norepinephrine has completely diffused. The closest electrodes also detect an increase in signal prior to those located across the subarray. Inset is an expanded view of the peak region showing the difference in both current and timing of the maximum. **Right)** A still image of the heat map was taken at the time indicated by the vertical dashed line on the inset plot. Oxidation potential of +0.6 V (vs. Pt). Data collection rate 100 Hz for all electrodes on subarray.

Due to the limitation of I/Os on the data acquisition system connected to the host computer, a maximum of 96 channels are available, allowing 96 out of 128 to be monitored at any given time. The next generation of the chip will have the ability to read all 128 electrodes through the expanded I/Os on a new data acquisition system on the host computer, eliminating this limitation. A current increase was observed as norepinephrine reached each electrode, with a 6.5, 5.6, and 4.9 nA increase relative to the baseline current occurring at the first exposed electrode, the electrode in the center of the subarray, and the last exposed electrode, respectively. The sequential decrease in signal across the array was a result of norepinephrine dilution throughout the diffusion process. After the 10-µL drop of 100 mM norepinephrine completely diffused into the media contained in the well, the norepinephrine reached a homogenous concentration of 4.8 mM, and the current of all electrodes equalized at 0.15 ± 0.08 nA (n = 96) greater than the media baseline. With a 10-ms time resolution for sampling, capture of the diffusion process is straightforward. The norepinephrine travelled across the diagonal of the subarray in 12 s, which is faster than pure diffusion (predicted to be 113 s),[46] likely due to advective flow caused by the addition of the norepinephrine solution with a

pipette. Monitoring the norepinephrine transport across a 250 µm × 250 µm subarray demonstrates that the spatial resolution of 30 µm, dictated by the electrode spacing, and the 10-ms time resolution, determined by the data collection frequency, allow the system to be used for imaging. Methods utilizing thorough mixing or microfluidic devices are currently being investigated to provide standardized calibration strategies that are independent of diffusion time or the technique of solution addition *via* pipette.

Norepinephrine diffusion across the array

The spatiotemporal resolution of the full array was studied by monitoring fluid transport controlled by combined head pressure and diffusion. A norepinephrine solution containing dye was used to correlate electrochemical images of norepinephrine with optical images of dye during transport across the array. Representative images can be seen in Figure 5.12, and the complementary video is linked at http://sites.chem.colostate.edu/henrylab/cmosvideo3.html. A baseline signal (t = 0 s) was collected for approximately one minute before the norepinephrine reached the array. After 88 s, the difference in head pressure between the reservoirs drove the norepinephrine over approximately the first half of the array, with diffusion generating a concentration gradient observed in both the electrochemical heat map and the optical images. Averaging the signal from all electrodes resulted in 1.3 nA distributed across the array as shown in the electrochemical heat map. After additional fluid transport across the array (t = 220 s), the average signal increased to 5.3 nA with the spatial distribution displayed in the electrochemical heat map. These results demonstrate that the array, which is of suitable size for chemically imaging cells in tissue slices, is capable of achieving high spatiotemporal resolution for the detection of electrochemically active species.

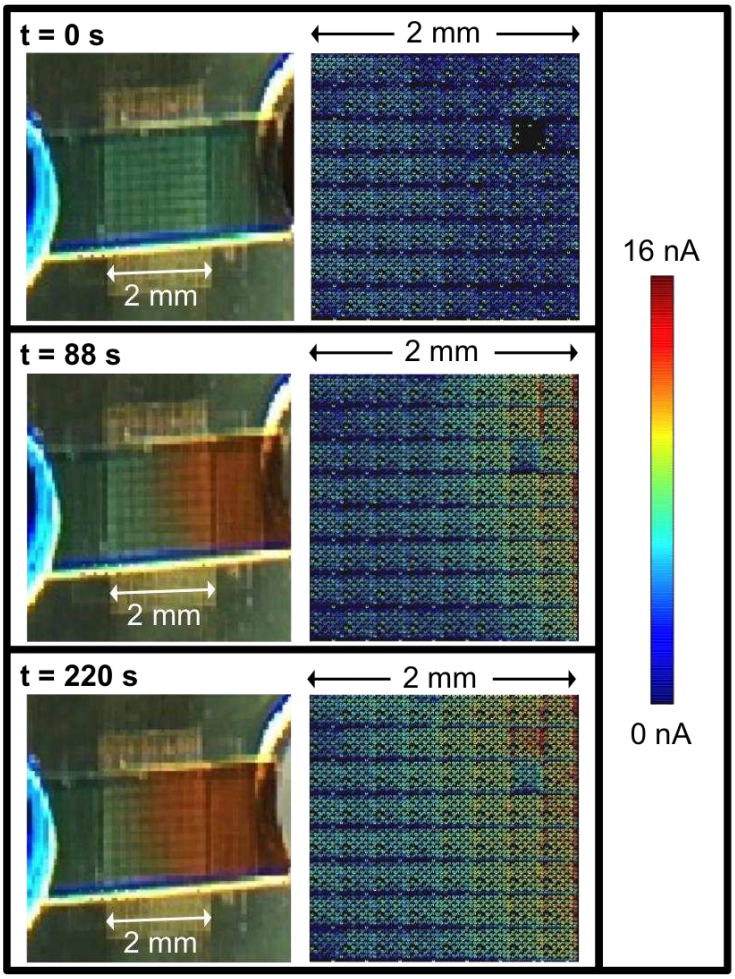

Figure 5.12: Diffusion of norepinephrine across the array. Optical images and electrochemical heat maps were recorded at the times indicated. Solutions contain dye for visualization. Red solution contains norepinephrine dissolved in neurobasal media, and blue solution is only neurobasal media. Oxidation potential of +0.6 V (vs. Pt). Data collection rate 100 Hz for all electrodes on active subarray. Switching rate between subarrays 1 Hz.

Bimodal distribution of norepinephrine

A bimodal gradient of norepinephrine was generated to electrochemically image a controlled chemical distribution over the electrode array. A Y-shaped microfluidic channel was used to direct 10 mM norepinephrine over approximately half of the array while the remaining portion of the array was exposed to media without norepinephrine. A representative electrochemical heat map and corresponding video frame is shown in Figure 5.13. A signal gradient was observed across each individual subarray, with the highest signal (44 ± 4 nA) on the left-most column, and lowest signal (23 ± 7 nA) to the right. The current decrease is the

result of analyte depletion from upstream electrodes as the norepinephrine flowed from left to right. This phenomenon was not observed across the array as a whole because the on-chip potentiostat cycled through each subarray at a rate of 1 Hz and the linear flow velocity (6.4 mm s^{-1}) was great enough that the solution was refreshed prior to cycling neighboring horizontal subarrays. The vertical position of the interface between the media and the norepinephrine was observed in the heat map to fluctuate by <250 µm with each column of subarrays. The position changed in the 8 s required to cycle to neighboring subarrays due to imperfect fluid control by the syringe pumps.

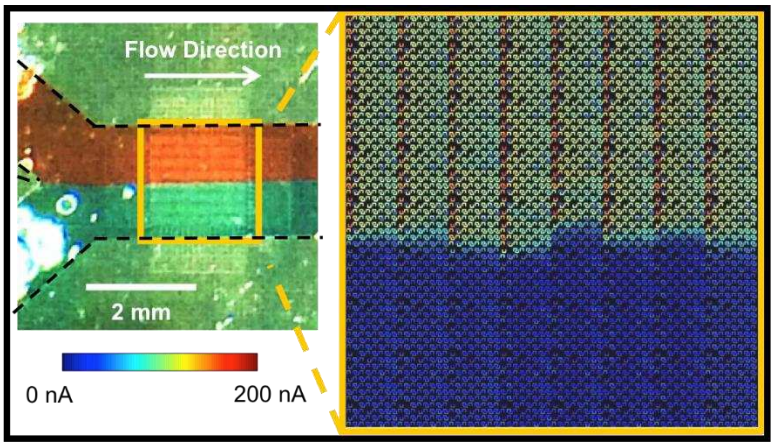

Figure 5.13: Optical image of bimodal gradient over the 2 mm × 2 mm microelectrode array and corresponding electrochemical heat map. Solutions contain dye for visualization. Red solution contains norepinephrine dissolved in neurobasal media, and blue solution is only neurobasal media. Dashed black lines indicate walls of microfluidic channel. Signal gradient across individual subarrays is due to analyte depletion by upstream electrodes. Oxidation potential of +0.6 V (vs. Pt). Data collection rate 100 Hz for all electrodes on active subarray. Switching rate between subarrays 1 Hz.

Control of the interface position was achieved by adjusting volumetric flow rates on the corresponding syringe pumps to demonstrate the spatiotemporal resolution capabilities of the system. A video of the resulting electrochemical heat map is linked at http://sites.chem.colostate.edu/henrylab/cmosvideo2.html and representative heat maps at each interface position can be seen along the top of Figure 5.14.

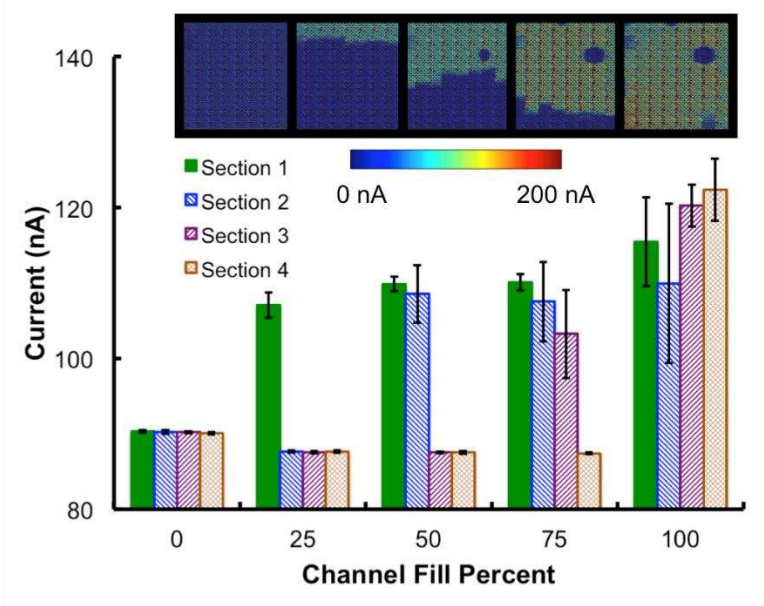

Figure 5.14: Average signal for rows of subarrays when a bimodal gradient of norepinephrine is generated over different sections of the array. Error bars represent signal standard deviation across the row of subarrays (n = 8). For simplicity, all signals were normalized to the maximum signal detected during the experiment. Heat maps corresponding to the signals plotted are shown at the top. In each x-axis category, the position of the data bar corresponds to the row of subarrays analyzed. Oxidation potential of +0.6 V (vs. Pt). Data collection rate 100 Hz for all electrodes on active subarray. Switching rate between subarrays 1 Hz.

For quantitative visualization, the signals were plotted as the average current from all electrodes in a horizontal row of eight subarrays representative of each of four sections of the array, with the error bars representing the standard deviation between the subarrays in the row. Each section of the array consists of two rows of subarrays, with Sections 1-4 ordered sequentially from the top of the array to the bottom. The plotted signals were taken after cycling through all 64 subarrays prior to starting the following cycle. A current increase of 23 $\pm$ 6 nA was observed to occur on the sections of the array exposed to norepinephrine and the timing correlated with the video. A bubble can be seen in Section 2 in the heat maps in Figure 5.14 when norepinephrine fills at least 50% of the channel, which can be correlated with the electrochemical video. The bubble prevented norepinephrine from reaching the surface of the electrodes, decreasing the average signal (110 nA compared to 120 nA) and resulting in a high standard deviation in signal (5-10% RSD) for the row of subarrays. Bubbles would be

problematic when imaging live tissue with this platform, so the design of the microfluidic device will be modified to control bubble formation and provide a method to interface live tissue slices with the electrode array. Monitoring the controlled distributions of norepinephrine and media in space and time demonstrates the ability of the electrode array to generate electrochemical images of gradients and correlate them to optical images with high spatiotemporal resolution, which could provide the ability to image neurotransmitter release from a tissue slice with cellular resolution, elucidating the effects of molecular gradients on cell-to-cell communication and other biological processes.

Conclusions

High-density electrode arrays containing large numbers of electrodes have primarily been used for impedance or voltage-based sensing with limited utilization of amperometric detection. The system described here was designed to augment traditional microscopy methods, offers an additional tool for imaging chemical distributions in biological systems, and has been used to electrochemically image distributions of norepinephrine standard solutions as a model neurotransmitter. The microelectrode array described is composed of 8,192 platinum working electrodes in a 2 mm × 2 mm area. PDMS microfluidics provided fluid control over the array to image distributions of norepinephrine. The density of the electrode array provided 30-µm spatial resolution, while the on-chip potentiostat and on-board electronics allowed norepinephrine detection with a maximum temporal resolution of 10 ms, as demonstrated by monitoring diffusion of norepinephrine across a single subarray. A larger area of 2 mm × 2 mm could be monitored by switching through subarrays at a rate of 1 Hz. This electrochemical imaging system will be implemented in the future for monitoring chemicals released from live tissue slices with 30 µm spatial resolution. This system has the potential to elucidate the effects of chemical gradients on biological processes such as chemotaxis, cancer metastasis, and directed cell migration.

This work is supported in part by National Science Foundation Grant No. GDE-0841259. The silicon-based microelectrode chip was manufactured by Avago Technologies. Their technical assistance and generous support for this project are greatly appreciated.

REFERENCES

1. B. J. Kim and M. M. Wu, *Annals of Biomedical Engineering*, 2012, **40**, 1316-1327.

2. R. A. Firtel and C. Y. Chung, *Bioessays*, 2000, **22**, 603-615.

3. W. J. Rosoff, J. S. Urbach, M. A. Esrick, R. G. McAllister, L. J. Richards and G. J. Goodhill, *Nature Neuroscience*, 2004, **7**, 678-682.

4. S. D. Nathanson, *Cancer*, 2003, **98**, 413-423.

5. B. Brucher and I. S. Jamall, *Cellular Physiology and Biochemistry*, 2014, **34**, 213-243.

6. N. C. Guerineau and M. G. Desarmenien, *Cellular and Molecular Neurobiology*, 2010, **30**, 1425-1431.

7. S. C. Ge, S. Koseoglu and C. L. Haynes, *Analytical and Bioanalytical Chemistry*, 2010, **397**, 3281-3304.

8. K. T. Schomacker, J. K. Frisoli, C. C. Compton, T. J. Flotte, J. M. Richter, N. S. Nishioka and T. F. Deutsch, *Lasers in Surgery and Medicine*, 1992, **12**, 63-78.

9. W. R. Zipfel, R. M. Williams, R. Christie, A. Y. Nikitin, B. T. Hyman and W. W. Webb, *Proceedings of the National Academy of Sciences of the United States of America*, 2003, **100**, 7075-7080.

10. Y. Amoh, K. Katsuoka and R. M. Hoffman, *Current Pharmaceutical Design*, 2008, **14**, 3810-3819.

11. C. Kobbert, R. Apps, I. Bechmann, J. L. Lanciego, J. Mey and S. Thanos, *Progress in Neurobiology*, 2000, **62**, 327-351.

12. L. J. Kricka and P. Fortina, *Clinical Chemistry*, 2009, **55**, 670-683.

13. R. M. Caprioli, T. B. Farmer and J. Gile, *Analytical Chemistry*, 1997, **69**, 4751-4760.

14. A. C. Grey, A. K. Gelasco, J. Section, R. A. Moreno-Rodriguez, E. L. Krug and K. L. Schey, *Anatomical Record-Advances in Integrative Anatomy and Evolutionary Biology*, 2010, **293**, 821-828.

15. A. J. Wain, *Electrochemistry Communications*, 2014, **46**, 9-12.

16. S. Amemiya, J. D. Guo, H. Xiong and D. A. Gross, *Analytical and Bioanalytical Chemistry*, 2006, **386**, 458-471.

17. S. Bergner, P. Vatsyayan and F. M. Matysik, *Analytica Chimica Acta*, 2013, **775**, 1-13.

18. A. Selimovic, J. L. Erkal, D. M. Spence and R. S. Martin, *Analyst*, 2014, **139**, 5686-5694.

19. M. M. Mensack, J. B. Wydallis, N. S. Lynn, D. S. Dandy and C. S. Henry, *Lab on a Chip*, 2013, **13**, 208-211.

20. B. N. Kim, A. D. Herbst, S. J. Kim, B. A. Minch and M. Lindau, *Biosensors & Bioelectronics*, 2013, **41**, 736-744.

21. B. Zhang, M. Heien, M. F. Santillo, L. Mellander and A. G. Ewing, *Analytical Chemistry*, 2011, **83**, 571-577.

22. J. Wang, R. Trouillon, J. Dunevall and A. G. Ewing, *Analytical Chemistry*, 2014, **86**, 4515-4520.

23. D. J. Bakkum, U. Frey, M. Radivojevic, T. L. Russell, J. Muller, M. Fiscella, H. Takahashi and A. Hierlemann, *Nature Communications*, 2013, **4**, 12.

24. M. Sen, K. Ino, K. Y. Inoue, T. Arai, T. Nishijo, A. Suda, R. Kunikata, H. Shiku and T. Matsue, *Biosensors & Bioelectronics*, 2013, **48**, 12-18.

25. F. Heer, W. Franks, A. Blau, S. Taschini, C. Ziegler, A. Hierlemann and H. Baltes, *Biosensors & Bioelectronics*, 2004, **20**, 358-366.

26. S. Hafizovic, F. Heer, T. Ugniwenko, U. Frey, A. Blau, C. Ziegler and A. Hierlemann, *Journal of Neuroscience Methods*, 2007, **164**, 93-106.

27. U. Frey, U. Egert, F. Heer, S. Hafizovic and A. Hierlemann, *Biosensors & Bioelectronics*, 2009, **24**, 2191-2198.

28. K. Ino, W. Saito, M. Koide, T. Umemura, H. Shiku and T. Matsue, *Lab on a Chip*, 2011, **11**, 385-388.

29. T. Matsue, *Analytical Sciences*, 2013, **29**, 171-179.

30. J. Rothe, O. Frey, A. Stettler, Y. H. Chen and A. Hierlemann, *Analytical Chemistry*, 2014, **86**, 6425-6432.

31. I. A. Ges, R. L. Brindley, K. P. M. Currie and F. J. Baudenbacher, *Lab on a Chip*, 2013, **13**, 4663-4673.

32. J. Wang, R. Trouillon, Y. Q. Lin, M. I. Svensson and A. G. Ewing, *Analytical Chemistry*, 2013, **85**, 5600-5608.

33. M. K. Zhao, H. Wi, E. J. Lee, E. J. Woo and T. I. Oh, *Physics in Medicine and Biology*, 2014, **59**, 5831-5847.

34. W. Cunningham, K. Mathieson, F. A. McEwan, A. Blue, R. McGeachy, J. A. McLeod, C. Morris-Ellis, V. O'Shea, K. M. Smith, A. Litke and M. Rahman, *Journal of Physics D-Applied Physics*, 2001, **34**, 2804-2809.

35. E. Ferrea, A. Maccione, L. Medrihan, T. Nieus, D. Ghezzi, P. Baldelli, F. Benfenati and L. Berdondini, *Frontiers in Neural Circuits*, 2012, **6**, 14.

36. S. R. I. Gabran, M. T. Salam, J. Dian, Y. El-Hayek, J. L. P. Velazquez, R. Genov, P. L. Carlen, M. M. A. Salama and R. R. Mansour, *Ieee Transactions on Neural Systems and Rehabilitation Engineering*, 2014, **22**, 1072-1082.

37. L. J. Johnson, E. Cohen, D. Ilg, R. Klein, P. Skeath and D. A. Scribner, *Journal of Neuroscience Methods*, 2012, **205**, 223-232.

38. D. Jackel, U. Frey, M. Fiscella, F. Franke and A. Hierlemann, *Journal of Neurophysiology*, 2012, **108**, 334-348.

39. W. Pettine, M. Jibson, T. Chen, S. Tobet, P. Nikkel and C. S. Henry, *Ieee Sensors Journal*, 2012, **12**, 1187-1192.

40. R. M. Feeny, J. B. Wydallis, T. Chen, S. Tobet, M. M. Reynolds and C. S. Henry, *Electroanalysis*, 2014, **26**.

41. M. Duwe, T. Chen and Ieee, Seoul, SOUTH KOREA, 2011.

42. D. C. Duffy, J. C. McDonald, O. J. A. Schueller and G. M. Whitesides, *Analytical Chemistry*, 1998, **70**, 4974-4984.

43. Y. Sameenoi, M. M. Mensack, K. Boonsong, R. Ewing, W. Dungchai, O. Chailapakul, D. M. Cropek and C. S. Henry, *Analyst*, 2011, **136**, 3177-3184.

44. J. P. Davim, C. Oliveira, N. Barricas and M. Conceicao, *International Journal of Advanced Manufacturing Technology*, 2008, **35**, 875-879.

45. I. A. Choudhury and S. Shirley, *Optics and Laser Technology*, 2010, **42**, 503-508.

46. M. Ansari, S. Kazemi, M. A. Khalilzadeh, H. Karimi-Maleh and M. B. P. Zanousi, *International Journal of Electrochemical Science*, 2013, **8**, 1938-1948.

CHAPTER 6. THREE-DIMENSIONAL IMAGING OF SEALED MICROFLUIDIC CHANNELS USING AN OPTICAL PROFILOMETER AND COMPENSATING OBJECTIVE

Introduction

An optical profilometry method for measuring three-dimensional microfluidic channels within sealed devices using a compensating objective is described. Presently, only confocal microscopy can accurately measure channel dimensions in sealed microfluidic devices and is limited to only two dimensions. Complete microfluidic devices made from PMMA, PDMS, COC, glass, and calcium fluoride were all successfully imaged using optical profilometry and a compensating objective. Features inside of microfluidic channels including electrodes, ports, posts, mixers, and surface roughness can be imaged. In addition, channel dimensions can be accurately measured with different fluids filling the channel including air, water, acetonitrile, ethanol and dimethylsulfoxide after correcting for the refractive index of the fluid in the channel. We also report a comparison study using the optical profilometer compensating objective with an established infrared spectroscopy method for measuring internal channel dimensions in IR-transparent devices. The described method offers immediate value to the lab-on-a-chip community because it allows nondestructive, submicrometer, three-dimensional imaging of features within assembled microfluidic devices. The optical profilometry techniques reported here have allowed us to gain a better physical understanding of the microfluidics used in the devices in the rest of the body of work reported in this thesis. This work was a collaborative effort by John Wydallis, who did the imaging, and Scott Noblitt, who did the majority of the data analysis, and is currently unpublished in a scientific journal.

Analysis of channel dimensions is a necessary practice when pursuing research and development involving microfluidic devices because channel dimensions play a role in everything from back pressure to detection limits. The most common methods for obtaining spatial information of microfluidic features include optical microscopy, optical profilometry,

contact profilometry, and scanning electron microscopy. The main drawback of these techniques is that the channel must be open on one side to allow the technique to measure dimensions or in the case of confocal microscopy a fluorescent probe is needed. Therefore, these types of channel analyses are often completed before the microfluidic device is fully assembled or the completed device is fractured orthogonally to the channel to obtain spatial measurements. The non-destructive method described here allows for channel dimension measurements to be collected from completed devices and thus is attractive for many applications.

Optical profilometry is a powerful technique offering sub-micron resolution in the imaging plane perpendicular to the light source dimensions and sub-nanometer resolution in the vertical dimension.[1-6] Optical profilometry works by analyzing the interference pattern created by the constructive and destructive interference of light that arises when the distance between a reference surface inside the profilometer and the sample surface are equidistant from an internal beam splitter. Software packages can be used to analyze these light interference patterns to generate high-resolution three-dimensional images of the sample surface. While traditional optical profilometry measures over open surfaces, it is possible to use a compensating objective to measure through the top layer of a sealed device to give a high-resolution image of the internal faces of the channel.[7-9] A compensating objective works by inserting an identical thickness of the device material into a compartment in the objective. The main limitation of this technique is that the microfluidic device must be transparent to visible light on at least one side. Here, we report for the first time the use of a compensating objective to measure channel dimensions within a sealed microfluidic device. The approach works with many different materials in channels filled with either air or liquid and is attractive because it allows for non-destructive device characterization.

Experimental Section

A Zygo (Middlefield, CT) ZeScope optical profilometer with ZeMaps software in flim-scanning mode was used for all profilometry measurements. A 5× glass-compensating objective (Zygo, part# OMP-0553A) with a 1.41 mm × 1.06 mm field of view was used to make all measurements with the compensating objective.[7-9] A Bruker (Billerica, MA, USA) Hyperion 3000 Infrared (IR) microscope with a single-element mercury cadmium telluride (MCT) detector and accompanying OPUS software package was used to collect all IR data. Infrared interference patterns were fit to a sine wave using the LabView (National Instruments, Austin, TX) "Find Tone" algorithm, and the channel depth was then computed using equation 1, where *d* is channel depth, *f* is the frequency of the interference pattern (in wavenumbers, cm^{-1}), and *n* is the refractive index of the medium inside the channel (air, *n*=1.000).

(1) $$d = \frac{f}{2n}$$

Poly(dimethylsiloxane) (PDMS) (Sylgard 184, Dow Corning, Midland, MI) devices were fabricated using previously reported photolithography and soft lithography methods.[10] The IR-transparent devices were built using two 25-mm diameter CaF_2 plates (Crystran Ltd, Poole, UK). 500-µm wide fluidic channels of varying depths were made in the CaF_2 devices using polymeric spacers with a range of thicknesses.

Results and Discussion

The validation study for the compensating optical profilometer objective was performed by comparing channel depth measurements in CaF_2 devices using both the optical profilometer and the IR microscope. Figure 6.1 compares measured depth from the optical profilometer (OP) to the established infrared interference technique (IR) with 96 samples. The lower-right inset shows representative IR interference patterns for a range of thicknesses. Confidence bands (95%) for the regression are shown in green, and 95% prediction bands for single

measurements are given by the dashed blue lines. The expected intercept of zero agrees with the observed data. A slope of unity is expected, but a slope of 1.0169±0.0047 (95% confidence interval) was observed. Although the profilometer measured 1.7±0.5% higher than the IR transmittance method, this margin of error should be acceptable for most microfluidic applications and may be due to calibration uncertainties in the instruments. The IR technique is limited to IR-transparent devices whereas the OP only requires transparency to visible wavelengths and is therefore more applicable to traditional microfluidic materials. For this study, IR-transparent CaF_2 devices were used to allow measurements to be taken using both OP and IR techniques. Other devices fabricated from materials including poly(dimethylsiloxane) (PDMS), poly(methyl methacrylate) (PMMA), glass, and cyclic olefin copolymer (COC) were also successfully measured using the optical profilometer with the compensating objective. An example of a completed microfluidic gradient generator device[11] fabricated from PDMS can be seen in Figure 6.2. Other features including platinum micro-wire electrodes in a microfluidic bubble cell,[12] carbon paste electrodes,[11] and surface roughness in COC and PMMA microfluidics were imaged within devices but are not shown. It is important to note that the field of view of the compensating objective is orders of magnitude larger than SEM and the software package can be used to stitch together large images of microfluidic networks. This makes it possible and convenient to image entire microfluidic devices instead of only a few representative areas.

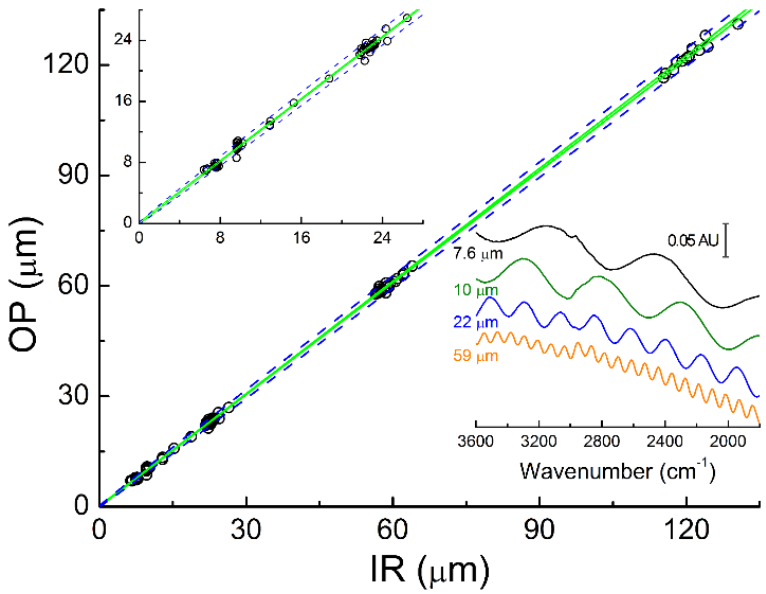

Figure 6.1: Correlation between optical profilometer (OP) and infrared transmittance (IR) thickness measurements. The weighted least-squares regression results were slope = 1.0169±0.0047, intercept = 50±120 nm, and R^2 = 0.99975. Regression was weighted by the average of the two measurements raised to the –1 power. 95% confidence bands are shown in green, and 95% prediction bands are shown in dashed blue. The upper-left inset shows data below 28 μm in detail, and the lower-right inset shows representative IR data.

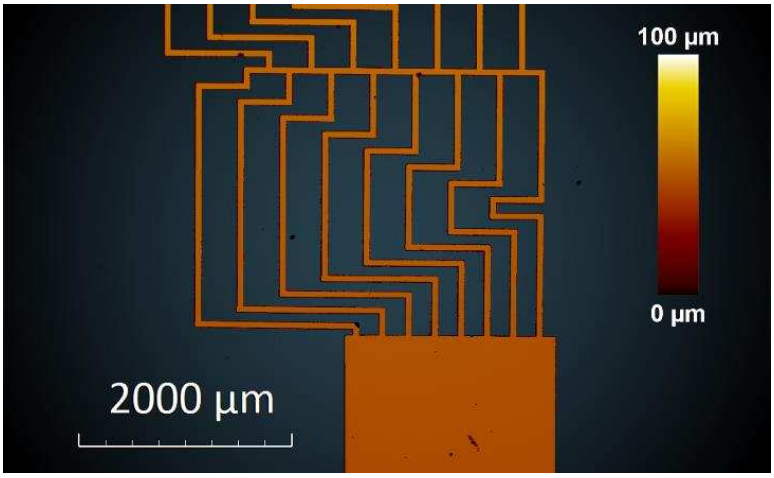

Figure 6.2: Image of a microfluidic gradient generator in a sealed PDMS device. The upper gradient feed channels are 100 μm wide, and the lower main channel is 2 mm wide. The channels were measured to be 48.5 μm wide. This image was compiled by stitching together multiple images taken using the compensating objective.

To further demonstrate the utility of this technique, overlapping microfluidic channels in a sealed PDMS device were imaged. A 500-μm wide PDMS channel was sealed orthogonally over a 75-μm wide PDMS channel to give three channel depths in a single device. Figure 6.3

shows the image of the overlapping channels. The channel in red is the 500-µm wide channel and had an average depth of 44.3 µm. The channel in green is the 75-µm wide channel that had an average depth of 23.9 µm. The area in blue is where the channels intersect and had an average measured depth of 68.2 µm as expected from the sum of the two intersecting channels. Figure 6.3 demonstrates that more complex, multi-layered, microfluidic devices can be measured using the compensating objective.

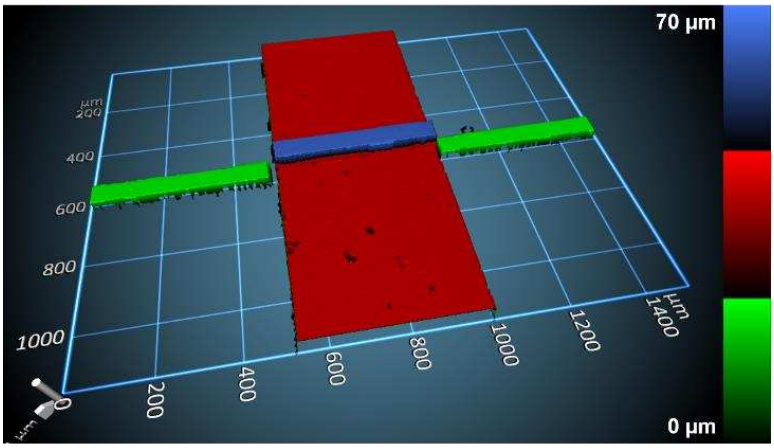

Figure 6.3: Three-dimensional image of channel thicknesses in a sealed two-layer PDMS device. The microfluidic channels intersect at a 90° angle. The wider channel in r ed is 500 µm wide and 44.3 µm deep. The thinner channel in green is 75 µm wide and 23.9 µm deep. The area in blue where these channels overlap had a measured depth of 68.2 µm, which is the sum of the two channel depths.

Another application of the optical profilometer's compensating objective is the ability to measure channel dimensions of liquid-filled channels. In order to accurately measure the channel dimensions, the compensating window in the objective must still contain the same material as the top layer of the device and the refractive index of the fluid in the device must be known. Figure 6.4 compares a microfluidic channel in a CaF_2 device with an average depth of 21.8 µm filled with air and water. After correcting for the refractive index of water (1.333) the average measured depth of the water-filled channel was 21.8 µm. The channel depth could also be measured when other fluids were present in the channel including acetonitrile, ethanol, and dimethylsulfoxide. However, as the refractive index of the fluid in the channel approaches the

refractive index of CaF_2 (1.434), the channel becomes more difficult to measure due to the lower amount of light being reflected at the fluid-substrate interfaces. Continuous topographical monitoring of a microfluidic channel filled with dynamic or static solutions has implications in studying film growth over time or three-dimensional movement of cell clusters.

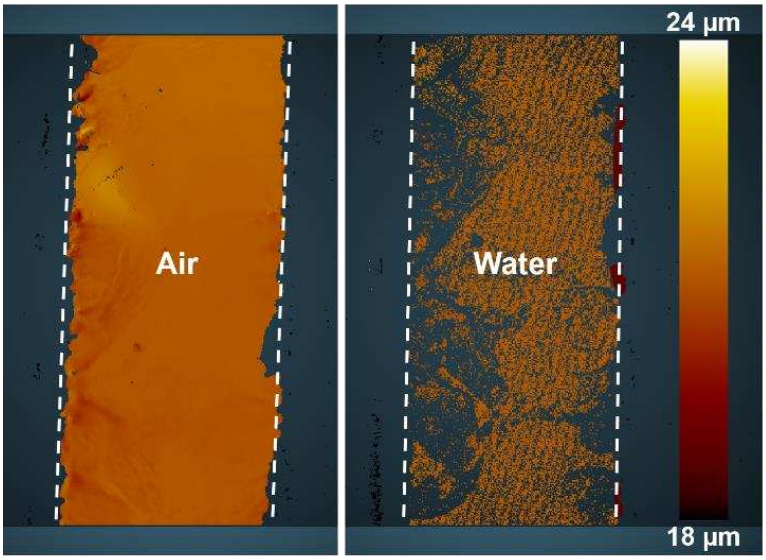

Figure 6.4: Profilometry of the same CaF_2 500-µm wide microfluidic channel filled with air (left) and with water (right). Channel boundaries are denoted by white dashed lines. The average measured channel depth when filled with air was 21.8 µm. The average measured depth of the channel when filled with water was 21.8 µm after correction for refractive index.

Conclusions

The technique described here allows direct measurement of microfluidic channel dimensions in sealed microfluidic devices. It was also shown that microfluidic channels filled with liquids can be topographically imaged. This opens up new interesting experiments as optical profilometers become more commonplace in research labs. Potential future projects that can be pursued using this technique include observing clusters of cells in a microfluidic device, film deposition over time in a dynamic microfluidic system, and imaging physical adhesion processes to substrates.

The authors gratefully acknowledge the Zygo Corporation especially Colin Quinn, John Fabio, and John Neff for their generosity and support of this research by lending the compensating objective to the Henry research group and providing consultation throughout the project. We would also like to thank the BP Exploration Operating Company Limited for financial support.

REFERENCES

1. Y. Fainman, E. Lenz and J. Shamir, *Appl Opt*, 1982, **21**, 3200-3208.

2. C. C. Huang, *OPTICE*, 1984, **23**, 365-370.

3. F. Laeri and T. C. Strand, *Appl Opt*, 1987, **26**, 2245-2249.

4. B. S. Lee and T. C. Strand, *Appl Opt*, 1990, **29**, 3784-3788.

5. D. Pantzer, J. Politch and L. Ek, *Appl Opt*, 1986, **25**, 4168.

6. G. E. Sommargren, *Appl Opt*, 1981, **20**, 610-618.

7. AMETEK, Optical Profiler Accessory Guide, 2014.

8. E. Felkel, Middlefield, CT, 2010.

9. Zygo, www.zygo.com/?/met/profilers, Accessed 2014.

10. D. C. Duffy, J. C. McDonald, O. J. Schueller and G. M. Whitesides, *Anal Chem*, 1998, **70**, 4974-4984.

11. M. M. Mensack, J. B. Wydallis, N. S. Lynn, Jr., D. S. Dandy and C. S. Henry, *Lab Chip*, 2013, **13**, 208-211.

12. S. D. Noblitt and C. S. Henry, *Anal Chem*, 2008, **80**, 7624-7630.

CHAPTER 7. CONCLUSION

The ability to image electroactive molecules that are invisible to other traditional methods offers a novel way to study chemical systems and biology. The development of an electrochemical imaging system was the driving force behind the work described in this thesis. Multiple approaches to the development of an electrochemical imaging system were pursued including carbon based electrodes integrated into a microfluidic network and design of a high-density platinum electrode array built on a CMOS microchip.

Carbon electrodes integrated into microfluidic networks

Carbon paste electrodes have been utilized in microfluidics because the paste can be spread into microfluidic channels for relative ease of integration into microfluidic networks when compared to solid metal electrodes. This work described how microfluidic chips containing carbon paste electrodes can be coupled to HPLC to measure reactive oxygen species. Furthermore, carbon paste electrodes were incorporated into a microfluidic device that could give four points of spatial resolution for quantitative detection of a distributed dopamine gradients.

CMOS based electrochemical imaging systems

Two separate CMOS microchip designs were described in this thesis. A preliminary, “generation one,” microchip was used to determine the optimal design and overall feasibility of using platinum microelectrodes to detect neurotransmitters. A second, “generation two,” CMOS microchip was designed based on the findings from the generation one microchips. The generation two CMOS microchips contained 8,192 individually addressable platinum microelectrodes and had an on-chip potentiostat and signal amplifiers. The generation two

CMOS microchip was used to map norepinephrine distributions over the 2 mm × 2 mm electrode array with spatiotemporal resolution.

Future Directions

The development and implementation of electrochemical imaging is still in its infancy as a quantitative technique, but with continued interest and improvements, electrochemical imaging could one day be widely utilized by the scientific and diagnostic communities. Risks that need to be addressed in future development of this imaging technology includes the preservation of electrode integrity under varying physical conditions. Currently the lifetime of CMOS microchips is at best a few hours in cell culture media making long term tissue studies difficult. Work in the Henry Laboratory is currently being done on how to coat the surfaces of the platinum microelectrodes to increase their lifetime in culture media without out compromising signal integrity.

Arrays of modified electrodes specific to various biomarkers has implications in the medical diagnostics world. A single drop of blood added to an array of thousands of microelectrodes each modified for electrochemical detection of a unique biomarker is a goal that I think warrants further research and development. It is my hope that new applications and further improvements to microelectrode arrays are continued in both academic and commercial settings.